Mon. Not. R. Astron. Soc. **385,** 1656–1672 (2008) doi:10.1111/j.1365-2966.2008.12955.x

The extragalactic radio-source population at 95 GHz

Elaine M. Sadler,[1⋆] Roberto Ricci,[2] Ronald D. Ekers,[3] Robert J. Sault,[4] Carole A. Jackson[3] and Gianfranco De Zotti[5,6]

[1]*School of Physics, University of Sydney, NSW 2006, Australia*
[2]*Department of Physics and Astronomy, University of Calgary, 2500 University Drive NW, Calgary AB, T2N 1N4, Canada*
[3]*Australia Telescope National Facility, CSIRO, PO Box 76, Epping, NSW 1710, Australia*
[4]*School of Physics, University of Melbourne, Victoria 3010, Australia*
[5]*SISSA/ISAS, Via Beirut 2-4, I-34014 Trieste, Italy*
[6]*INAF, Osservatorio Astronomico di Padova, Vicolo del'Osservatorio 5, I-35122 Padova, Italy*

Accepted 2008 January 11. Received 2008 January 8; in original form 2007 September 22

ABSTRACT

We have used the Australia Telescope Compact Array (ATCA) at 95 GHz to carry out continuum observations of 130 extragalactic radio sources selected from the Australia Telescope 20 GHz (AT20G) survey. We use a triple-correlation method to measure simultaneous 20- and 95-GHz flux densities for these objects, and over 90 per cent of our target sources are detected at 95 GHz. We demonstrate that the ATCA can robustly measure 95-GHz flux densities with an accuracy of ∼10 per cent in a few minutes for sources stronger than about 50 mJy.

We measure the distribution of radio spectral indices in a flux-limited sample of extragalactic sources, and show that the median 20–95 GHz spectral index does not vary significantly with flux density for $S_{20} > 150$ mJy. This finding allows us to estimate the extragalactic radio source counts at 95 GHz by combining our observed 20–95 GHz spectral-index distribution with the accurate 20-GHz source counts measured in the AT20G survey.

Our derived 95-GHz source counts at flux densities above 80 mJy are significantly lower than those found by several previous studies. The main reason is that most radio sources with flat or rising spectra in the frequency range 5–20 GHz show a spectral turnover between 20 and 95 GHz. As a result, there are fewer 95-GHz sources (by almost a factor of 2 at 0.1 Jy) than would be predicted on the basis of extrapolation from the source populations seen in lower-frequency surveys. We also derive the predicted confusion noise in cosmic microwave background surveys at 95 GHz and find a value 20–30 per cent lower than previous estimates.

The 95-GHz source population at the flux levels probed by this study is dominated by quasi-stellar objects with a median redshift $z \sim 1$. We find a correlation between optical magnitude and 95-GHz flux density which suggests that many of the brightest 95-GHz sources may be relativistically beamed, with both the optical and millimetre continuum significantly brightened by Doppler boosting.

Key words: techniques: interferometric – galaxies: active – quasars: general – cosmic microwave background – radio continuum: galaxies – radio continuum: general.

1 INTRODUCTION

The radio sky at 90–100 GHz remains largely uncharted territory. At frequencies above 5 GHz, traditional surveys of even modest areas of sky become impractical because of the small field of view of present telescopes. For example, the effective field of view of the NRAO VLA telescope is 0.22 deg^2 at 1.4 GHz, but less than 0.0002 deg^2 at its highest frequency of 50 GHz. Most radio telescopes designed to operate at millimetre wavelengths have similarly small fields of view,[1] so that blind surveys of large areas of sky are only possible by using specially designed instruments or techniques.

Fig. 1 summarizes the sensitivity limits of large-area radio continuum surveys which cover at least a quarter of the sky. There are presently only two large-area surveys above 5 GHz. The *WMAP* Point Source Catalogue (Bennett et al. 2003; Hinshaw et al. 2007) detects sources down to 0.8–1.0 Jy in five frequency bands from 23

⋆E-mail: ems@physics.usyd.edu.au

[1] In general, the area of sky covered by the primary beam of a radio telescope scales as ν^{-2} for increasing frequency ν.

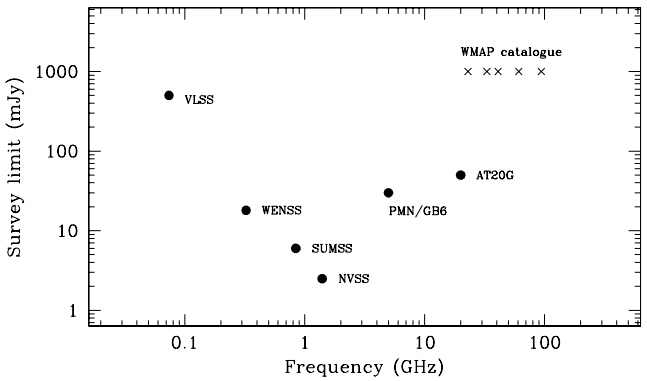

Figure 1. Detection limits of the most sensitive large-area radio surveys available at frequencies from 74 MHz to 94 GHz. Only surveys which cover at least 25 per cent of the sky have been included. The surveys plotted are the VLA Low-Frequency Sky Survey (VLSS, Cohen et al. 2007), Westerbork Northern Sky Survey (WENSS, Rengelink et al. 1997), Sydney University Molonglo Sky Survey (SUMSS, Bock, Large & Sadler 1999),NRAO VLA Sky Survey (NVSS, Condon et al. 1998), single-dish PMN and GB6 surveys (Griffith & Wright 1993; Gregory et al. 1996), AT20G (Ricci et al. 2004) and the *WMAP* extragalactic source catalogue (Hinshaw et al. 2007).

to 94 GHz. The Australia Telescope 20 GHz (AT20G) survey (Ricci et al. 2004; Sadler et al. 2006) uses a wide-band (8 GHz bandwidth) analogue correlator to scan the sky rapidly at 20 GHz, detecting sources down to a limit of ∼40 mJy, and presently represents the highest radio frequency at which a blind survey of a large fraction of the sky has been carried to a detection limit below 100 mJy.

There are several reasons why we would like to learn more about the extragalactic radio-source population at frequencies well above those probed by existing large-area surveys. Corrections for extragalactic foreground confusion (e.g. De Zotti et al. 2005) will be critical for next-generation surveys of the cosmic microwave background (CMB) like the *Planck* mission, which aims to measure CMB anisotropies on angular scales of 5–30 arcmin in the frequency range 30–350 GHz. Such corrections require an accurate knowledge of the foreground point-source population at frequencies of 30 GHz and above.

Observations at 95 GHz are particularly relevant to *Planck*, since the *Planck* 100-GHz channel and the nearby 143-GHz channel are the 'cleanest' ones for CMB studies in both temperature and polarization on small angular scales, where the main foreground contamination comes from extragalactic sources. The 100- and 143-GHz channels will also be the most sensitive *Planck* channels[2] (Lamarre et al. 2003), far exceeding the performances of *WMAP*, so that an accurate subtraction of point source contamination at these frequencies will be very important.

A second motivation arises, because present models of radio-galaxy evolution imply that very young radio sources (tens to hundreds of years old) should have radio spectra which peak above 5 GHz (the so-called gigahertz-peaked spectrum, or GPS sources; O'Dea 1998), with the spectra of younger sources peaking at progressively higher frequencies. Such objects are rare, since they represent a very short-lived evolutionary stage, but are predicted to be extremely luminous and hence easily detectable out to high redshift in high-frequency radio surveys. Until now, models for the luminosity evolution of young radio galaxies have been almost totally unconstrained by the available data, and the need for a large, homogeneously selected sample of GPS sources is well recognized (e.g. Snellen et al. 2000). An analysis of evolutionary properties of GPS galaxies has recently been carried out by Tinti & De Zotti (2006).

In addition to these science goals, 95-GHz observations are relevant to the calibration strategy for the Atacama Large Millimetre Array (ALMA; De Breuck 2005), which will need to do rapid switching between object and calibrators to achieve the required phase stability. This ideally requires a network of calibrators no more than 1°–2° apart and stronger than 50–100 mJy at 90 GHz. The existing proposal (Holdaway, Carilli & Laing 2004) is to find 90-GHz calibrators by selecting candidates from low-frequency (1–5 GHz) surveys and using ALMA itself to measure their 90-GHz flux density. We have already suggested (Sadler et al. 2006) that a more efficient alternative would be to select ALMA calibrators from the high-frequency AT20G survey. One aim of this study is therefore to measure the surface density of AT20G sources at 90–100 GHz.

Early work in this area dates back to the 1970s. Owen et al. (1978) used the NRAO 11-m radio telescope at Kitt Peak to measure the 90-GHz flux density of 237 strong sources which were known to have flat or inverted radio spectra at centimetre wavelengths. They also made near-simultaneous observations of about 100 of these sources at 1.4, 4.6, 15 and 22 GHz using dishes of the NRAO VLA. Their main findings were that most of their sources had flat spectra ($\alpha \sim 0$) over the whole frequency range 1–90 GHz, and that the level of radio variability at 90 GHz was lower than expected (most sources varied by less than 30 per cent on a one-year time-scale). Owen, Helfand & Spangler (1981) observed 25 strong extragalactic millimetre sources at ∼1 keV with the *Einstein* X-ray obsetvatory, and found a strong correlation between their X-ray and 90-GHz flux densities. They noted that this is consistent with a synchrotron self-Compton model in which the X-ray emission arises from the Compton scattering of millimetre radio photons off the relativistic electrons which created them.

Steppe et al. (1988) observed a sample of 294 strong (>1 Jy at 5 GHz) extragalactic sources at 90 GHz with the IRAM 30-m telescope, and also measured 20–90 GHz spectral indices for a subset of these objects. They found that only about 5 per cent of compact, flat-spectrum radio sources had inverted ($\alpha > 0.1$) spectra at 20–90 GHz, and that most of these were variable sources undergoing an outburst.

More recent continuum work at 90–100 GHz has mainly focused on variability studies of targeted samples of objects such as quasi-stellar objects (QSOs) and blazars (e.g. Landau, Epstein & Rather 1980; Teräsranta et al. 2004; Hovatta et al. 2007). All these studies have been based on sources pre-selected at frequencies of 5 GHz or below. The *WMAP* catalogue (Hinshaw et al. 2007) provides the first complete sample of radio sources selected in the 90-GHz band, but only 121 out of the 323 discrete sources listed in the three-year catalogue are detected at 94 GHz (limiting flux density 0.8 Jy).

Throughout this paper, we use $H_0 = 70$ km s^{-1} Mpc^{-1}, $\Omega_{\rm m} = 0.3$ and $\Omega_\Lambda = 0.7$.

2 AUSTRALIA TELESCOPE COMPACT ARRAY 95-GHz OBSERVATIONS

The data analysed in this paper were obtained at the Australia Telescope Compact Array (ATCA) in two observing runs during 2005 and 2006 (see Table 1 for details of the observations).

[2] Although the quoted *Planck* sensitivity ($\Delta T/T$ per pixel) is slightly better at 30 GHz than at 100 and 143 GHz, the smaller pixel size (in arcmin) at high frequencies means that the 100- and 143-GHz channels are far more sensitive when scaled to the same angular resolution.

Table 1. Log of our ATCA observations at 95 GHz.

Date	ATCA	$\nu_{\rm cen}$	Notes
2005 July 1–3	H75A	18.8, 21.1, 93.5, 95.6	2×24 h
2006 September 16–19	H75A	18.8, 21.1, 93.5, 95.6	3×12 h

Table 2. Sample selection for the 2005 and 2006 runs. All targets were also chosen to lie in the declination range -30° to -50° to ensure that they could be observed at low airmass.

Run	N	20-GHz flux density	Spectral index cut	Notes
2005	59	>50 mJy	$\alpha_8^{20} > 0$	'Inverted spectrum'
2005	9	>300 mJy	...	AT calibrator sample
2006	70	>150 mJy	...	Flux-limited sample

The ATCA was used in mosaic mode to minimize the slewing time between sources, with the target sources observed in groups of five to seven objects which were close (within about 10° on the sky) in both right ascension and declination.

2.1 Sample selection

All our target sources were selected from the AT20G survey of the southern sky (Ricci et al. 2004; Sadler et al. 2006) as noted in Section 1. The target selection criteria were different in 2005 and 2006, and are summarized in Table 2.

An important feature of the AT20G survey is that sources selected at 20 GHz are also observed near-simultaneously at 5 and 8 GHz, so that radio spectral indices measured in the 5–20 GHz frequency range are not affected by variability. A recent description of the AT20G data pipeline is given by Massardi et al. (2008).

In 2005 July, we observed a sample of 59 sources selected from the AT20G survey to have inverted (rising) radio spectra between 8 and 20 GHz. Nine strong AT20G sources which are ATCA calibrators were also observed to provide a consistency check on our final flux density scale at 95 GHz. All these sources were also chosen to lie at declinations between -30° and -50° to ensure that they could be observed at low airmass. Our aim was to see how many of the 'inverted-spectrum' AT20G sources showed a high-frequency turnover above 20 GHz and so were candidates for extreme GPS sources.

In 2006 September, we observed a flux-limited ($S_{20} > 150$ mJy) sample of 70 AT20G sources, again between declination -30° and -50°. Our aim here was to use the distribution of 20–95 GHz radio spectral indices to estimate the overall surface density of extragalactic radio sources at 95 GHz. Eight sources belonged to both the 2005 and 2006 samples, giving a total of 130 individual sources with 95-GHz measurements in the two-year programme.

2.2 Antenna configuration and observing frequencies

We used the ATCA in its most compact configuration, the hybrid H75A array, which has a maximum baseline of 75 m and is designed to provide good *uv* coverage and phase stability for short observations at millimetre frequencies. The ATCA field of view is roughly 2.5 arcmin at 20 GHz and 30 arcsec at 95 GHz, and the angular resolution in the H75 array is around 40 arcsec at 20 GHz and 10 arcsec at 95 GHz.

Since one of our goals was to measure reliable 20–95 GHz spectral indices for the AT20G sources, and some AT20G sources are known to be variable at 20 GHz (Sadler et al. 2006), we observed all our target sources at both 20 and 95 GHz in the 2005 and 2006 runs. The observing frequencies (IFs) listed in Table 1 were selected to lie in regions where the ATCA receivers have their best $T_{\rm sys}$ performance.

2.3 Calibration techniques

At the time of these observations the ATCA 3-mm system did not have a noise diode, so to place visibility amplitudes on a temperature scale a vane (paddle) needed to be interposed in front of the receiver in the antenna vertex room at regular intervals for $T_{\rm sys}$ calibration. This was done at the start of each observing session, and also repeated just before starting the observation of each source group (at intervals of about half an hour).

2.3.1 Flux density calibration

At 20 GHz, the absolute flux density scale was set using the standard ATCA primary calibrator PKS 1934−638. At 95 GHz, however, PKS 1934−638 is far too weak to provide a reliable calibration of the flux density scale. We therefore followed the usual practice and used the planet Uranus as our flux calibrator at 95 GHz. Although the angular size of this planet is significantly smaller than the ATCA beam, it cannot be assumed to be a point source. A model of its intensity as a function of frequency and baseline length is therefore used to perform the calibration. To minimize any gain-elevation effects (i.e. possible variations in antenna efficiency as a function of elevation) on the primary calibration, we always observed the planet close to transit and followed or preceded by a target source group at a similar elevation.

2.3.2 Antenna pointing calibration

The ATCA primary beam at 95 GHz is only 30 arcsec full width at half-maximum, and the pointing and tracking requirements for operation at this high frequency have been discussed in detail by Kesteven (1998). The effects of a pointing offset can be seen in Fig. 2. The main factors affecting the positional accuracy of the ATCA are pointing and tracking errors (typically 1.5 arcsec rms on each axis when reference pointing is used), atmospheric fluctuations (up to 3.0 arcsec rms for sources observed close to the zenith), and wind loading (which starts to have a significant effect when the wind

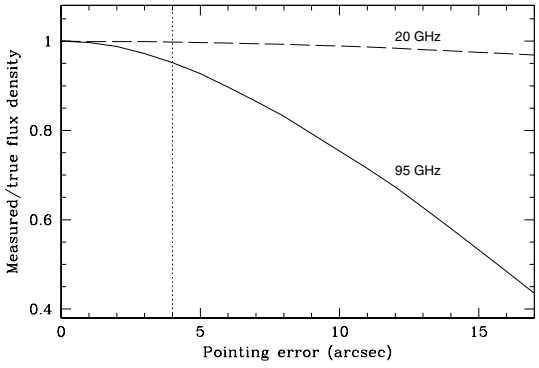

Figure 2. The effect of antenna pointing errors on the measured flux density at 20 and 95 GHz. For our 2005 and 2006 runs, pointing and tracking errors are expected to be less than 4.0 arcsec (shown by the dotted vertical line), except on rare occasions when the wind is both strong and gusty. Pointing and tracking errors should therefore have at most a small effect on the measured flux densities and 20–95 GHz spectral index distribution.

speed rises above 10–15 km h^{-1}, especially when conditions are gusty). Also contributing to the error budget is the uncertainty in the individual AT20G source positions (typically less than 1.0 arcsec).

The uncorrected ATCA antenna pointing errors in typical observing conditions can be up to 20 arcsec. It is therefore essential to use reference pointing when observing at high frequencies. A reference pointing check using a strong phase calibrator was therefore done whenever moving to a new source group. This allowed a new pointing solution to be calculated and applied to the sources in each group, reducing the final pointing errors to a few arcsec or less. We generally did our reference pointing calibrations at 20 GHz rather than 95 GHz, because the higher signal-to-noise ratio and larger field of view at 20 GHz allows a more accurate solution.

2.4 2005 observing run

Both the effective detection limit for continuum sources at 95–100 GHz and the accuracy of the derived flux densities are strongly affected by atmospheric transparency, phase stability and decorrelation, and the general performance of the ATCA 3-mm system for weak continuum sources was unknown at the time of our 2005 run. We therefore took a conservative approach and repeated the same set of observations on each of the two days we were allocated.

Since all our target sources were known (from AT20G images at 20 GHz) to be point sources at high frequency, we chose to measure flux densities using a triple-correlation technique rather than imaging our target fields. The triple-correlation technique is discussed briefly in Section 3 of this paper, and in more detail in a companion paper by Ricci, Sault & Ekers (in preparation).

In the 2005 run, each group of target sources was observed three times at different hour angles to provide a range in *uv* coverage. The total integration time for each source at 95 GHz was 3×4 min on each day. On the second day, each group of sources was observed at both 95 and 20 GHz, with the total observing time at 20 GHz being 3×1 min. To minimize the effects of airmass, all observations were made at hour angles less than ± 1.5 h from the zenith.

2.5 2006 observing run

During our 2005 run, we found that observing conditions at 95 GHz were significantly better at night than during the day. This appears to be generally the case at the ATCA, even during the winter months, as discussed recently by Middelberg, Sault & Kesteven (2006). We therefore chose to carry out our 2006 observing campaign in three consecutive 12 hr nighttime slots. The array configuration and frequency set-up were the same as in 2005.

Our 2006 sample of 70 AT20G sources was split into nine groups which were observed at 20 and 95 GHz on either the first or the second nights. Each source was observed between two and four times, with the integration time for each observation being 80 s at 95 GHz and 40 s at 20 GHz. The integration times were shorter than in 2005, because most of the 2006 sources were significantly brighter at 20 GHz than those observed in 2005. On the third night, we reobserved 32 sources which did not appear to show an obvious 95-GHz detection on the first two days. These objects were reobserved for 3 min cuts at 95 GHz.

3 DATA REDUCTION

The raw visibility data were reduced using the astronomical software package MIRIAD (Sault, Teuben & Wright 1995). The 95- and 20-GHz bandpasses were calibrated using the strong ATCA high-frequency calibrator PKS 1921−293.

3.1 Flux density measurements

Atmospheric turbulence creates strong phase instability in the 95-GHz band and target sources and phase calibrators need to be switched very frequently (i.e. on time-scales of a few minutes or less) to avoid the loss of total intensity flux through phase decorrelation.

Because of the large number of sources we wanted to observe in both 2005 and 2006, it would have been difficult to spend enough time on phase calibrators to correct for phase decorrelation in the standard way. We therefore chose not to observe any secondary (phase) calibrators in our 2006 run. Instead, we chose to reduce our 2005 and 2006 data using the triple-correlation (phase closure) method as noted earlier.

The triple-correlation method has also been used by Sault et al. when monitoring flux densities of ATCA calibrators at 3 mm, and is robust against phase variations during the target observation. It is described in detail by Cornwell (1987) and Thompson, Moran & Swenson (2001). The application of this technique to ATCA millimetre data is discussed by Ricci, Sault & Ekers (in preparation), who have also used a set of Monte Carlo simulations to test the robustness of this technique for the detectability and flux density measurements of the 95-GHz data presented in this paper.

Table 3 lists the estimated flux density errors for our 2005 and 2006 data. These were calculated from the scatter in the triple-correlation amplitudes by taking different scans and different spectral windows (IFs) of the same source separately. At 20 GHz, the flux density errors are significantly higher in 2006 than in 2005. This is probably because the 2005 20-GHz data were taken in very good observing conditions, whereas the 2006 data at the same frequency were much noisier.

3.2 Data tables

Tables 4 and 5 list the individual sources observed at 20 and 95 GHz in our 2005 and 2006 runs. The main information contained in these tables is as follows.

(i) The AT20G working name, used to track individual sources through the data pipeline. A letter 'C' after the name indicates that the source is also an ATCA calibrator.

(ii) The J2000 radio position of the source, measured from AT20G 20-GHz images.

(iii) Alternate source name, where available.

(iv) Blue (B_J) magnitude of the optical counterpart if any, from the Supercosmos catalogue (Hambly et al. 2001). As discussed in Section 4.7, an optical object is accepted as the radio ID if it lies within 2.5 arcsec of the AT20G radio position.

(v) Supercosmos classification of the optical ID, where 1 indicates a galaxy and 2 a stellar object (candidate QSO).

Table 3. Error estimates for the flux densities measured in 2005 and 2006, derived using the methods of Ricci, Sault & Ekers (in preparation).

	Flux density error estimates	
	20 GHz	95 GHz
2005	5.4 per cent	11.8 per cent
2006	10.7 per cent	10.2 per cent

Table 4. Table of 2005 observations. 'C' after the source name in the first column indicates an ATCA calibrator, and * indicates a source within 10° of the Galactic plane (optical *B* magnitudes are not listed for these objects).

Name	Radio position	Alternate name			2005		2005	2004		2004		2004		NVSS		SUMSS			
			B_J	T	S_{95}		S_{20}	S_{20}	±	$S_{8.6}$	±	$S_{4.8}$	±	$S_{1.4}$	±	S_{843}	±	z	ID
	(J2000)		mag		Day1	Day2	mJy	mJy		mJy		mJy		mJy		mJy			
(a) Sources with inverted radio spectra at 5–20 GHz																			
0026−3512	00 26 16.39 −35 12 48.5	PMNJ 0026−3512	22.24	1	1155	1119	1273	1123	20	357	22	136	5	25.0	0.9	12.2	1.5	...	
0044−3752	00 44 17.06 −37 52 59.2	PMNJ 0044−3752	20.30	2	74	87	91	114	3	86	5	66	2	18.8	0.7	47.3	1.9	...	
0106−4034C	01 06 45.11 −40 34 19.5	WMAP 171	18.60	2	1789	1775	2632	2146	79	1549	38	1009	77	...	..	650.9	19.6	0.584	Q
0111−4749	01 11 02.94 −47 49 11.4	2dFGRS S834Z009	18.86	1	<99	<64	71	83	3	64	2	30	3	...	..	19.2	2.9	0.1542	G
0127−4813	01 27 14.87 −48 13 32.1	PMNJ 0127−4813	19.91	1	251	232	200	237	9	181	5	140	10	...	..	80.8	2.6	...	
0136−4044	01 36 02.88 −40 44 50.4	PMNJ 0136−4044	21.36	2	355	344	380	350	11	273	7	226	16	...	..	115.1	3.6	...	
0142−4206	01 42 07.29 −42 06 01.8	...	20.64	1	67	60	84	131	5	97	3	58	4	...	..	29.3	2.4	...	
0143−3200	01 43 10.15 −32 00 55.7	PKS 0140−322	19.89	2	405	389	401	517	16	341	8	293	21	76.1	2.3	106.6	3.7	0.375	Q
0421−4818	04 21 27.49 −48 18 05.2	PKS 0419−484	16.85	2	295	300	513	452	13	356	9	232	2	...	..	284.8	8.6	0.527	Q
0427−3901	04 27 21.69 −39 01 00.1	PMNJ 0427−3900	19.33	2	75	65	126	159	5	131	3	112	1	141.8	4.3	135.2	4.2	...	
0428−4357	04 28 10.11 −43 57 46.4	PMNJ 0428−4358	>22	0	44	60	110	114	3	101	3	57	1	...	..	10.8	1.1	...	
0433−4502	04 33 13.89 −45 02 54.6	PMNJ 0433−4503	19.77	1	109	105	96	144	4	117	3	89	2	...	..	53.0	1.8	...	
0434−4211	04 34 45.34 −42 11 07.9	PMNJ 0434−4211	21.75	2	145	158	208	165	4	58	2	53	1	...	..	137.6	4.2	...	
0440−4732	04 40 23.74 −47 32 18.7	...	22.73	2	47	41	69	61	2	20	1	8	1	...	..	<5.0	..	...	
0451−4936	04 51 02.68 −49 36 26.9	...	20.26	2	69	73	141	147	4	123	3	89	2	...	..	46.3	1.7	...	
0455−4615C	04 55 50.79 −46 15 58.7	WMAP 151	17.89	2	3081	3071	4420	4157	121	3606	90	2613	20	...	..	2874.0	86.3	0.853	Q
0506−4310	05 06 03.81 −43 10 58.4	PMNJ 0506−4310	22.47	2	<69	<66	50	111	4	96	2	77	2	...	..	111.8	3.5	...	
0516−3703	05 16 34.80 −37 03 32.7	PMNJ 0516−3704	19.73	2	<81	<63	73	73	2	56	1	46	1	25.1	1.0	15.3	1.4	...	
0522−4020	05 22 54.12 −40 20 31.0	PKS 0521−403	20.42	2	118	124	329	349	16	280	4	221	2	...	..	303.0	9.2	...	
0523−2955	05 23 00.12 −29 55 17.3	PMNJ 0522−2955	21.27	1	61	50	83	79	4	59	2	57	1	212.3	4.0	225.0	9.9	...	
0532−3848	05 32 02.14 −38 48 54.3	PMNJ 0532−3848	19.40	2	197	192	271	235	10	190	3	131	2	168.6	5.1	139.8	4.4	...	
0538−4405C	05 38 50.35 −44 05 08.6	WMAP 148	15.77	2	8051	8076	7328	5294	224	4231	60	3800	35	...	..	3524.0	105.8	0.894	Q
0552−4522	05 52 10.00 −45 22 24.6	PMNJ 0552−4522	18.36	2	117	133	227	237	10	173	3	143	2	...	..	248.3	7.7	...	
0559−4529	05 59 11.53 −45 29 40.5	PKS 0557−454	18.34	2	546	576	797	606	27	422	6	321	3	...	..	407.9	12.3	0.687	Q
0608−3041	06 08 40.59 −30 41 33.8	PKS 0606−306	17.83	2	82	81	124	99	3	73	5	67	5	257.5	8.7	325.5	12.2	0.2237	Q
1102−4404	11 02 04.88 −44 04 22.3	PKS 1059−438	20.13	2	463	493	488	765	20	703	19	566	11	...	..	111.0	3.6	...	
1109−4815	11 09 18.96 −48 15 18.7	PMNJ 1109−4815	21.29	1	315	335	342	335	9	157	7	170	3	...	..	193.5	5.9	...	
1117−4838	11 17 20.01 −48 38 09.8	PMNJ 1117−4838	21.28	2	114	135	146	204	5	127	4	96	2	...	..	97.1	4.7	...	
1149−3723	11 49 01.83 −37 23 44.0	PMNJ 1149−3724	19.78	2	<90	<73	50	73	3	77	3	73	2	71.8	2.2	82.0	2.7	...	
1427−3305	14 27 41.55 −33 05 32.0	WMAP 193	20.46	2	1471	1471	871	770	21	606	17	363	10	161.0	4.9	187.1	6.2	...	
1454−3747C	14 54 27.57 −37 47 32.8	PKS 1451−375	16.36	2	947	993	1151	1891	49	792	22	656	16	942.7	28.3	2045.0	61.4	0.3142	Q
1616−4018*	16 16 59.63 −40 18 04.3	PMNJ 1617−4017	—	–	95	86	120	100	3	72	2	66	2	...	..	48.7	1.9	...	
1624−4206*	16 24 58.72 −42 06 57.1	PMNJ 1625−4207	—	–	62	56	68	75	3	48	2	35	1	...	..	33.4	1.7	...	
1710−4718*	17 10 43.99 −47 18 20.3	...	—	–	<93	<70	62	76	4	28	1	16	1	...	..	...	..	...	
2113−3838	21 13 53.91 −38 38 27.3	...	18.45	2	<98	63	94	101	4	71	5	59	2	44.6	1.5	57.2	2.0	0.850	Q
2151−3027C	21 51 55.56 −30 27 53.3	PKS 2149−306	17.95	2	621	688	2108	1846	58	1314	73	1302	36	1243.6	37.3	1088.0	32.7	2.345	Q
2259−4818	22 59 26.26 −48 18 25.3	PMNJ 2259−4818	18.35	1	60	82	79	72	3	69	17	47	2	...	..	54.5	2.2	0.1708	G

Table 4 – *continued*

Name	Position (J2000)	Alternate name	2005 S_{95} Day1	2005 S_{95} Day2	2005 S_{20} mJy	2004 S_{20} mJy	±	2004 $S_{8.6}$ mJy	±	2004 $S_{4.8}$ mJy	±	NVSS $S_{1.4}$ mJy	±	SUMSS S_{843} mJy	±	z	ID
(b) Other sources observed but later removed from the 'inverted spectrum' sample																	
0459−4528	04 59 21.11 −45 28 45.7	PMNJ 0459−4529	<67	<78	45	76	2	60	2	70	2	...	..	244.3	7.5	...	
0537−3357	05 37 32.14 −33 57 55.2	...	<86	<58	61	74	3	50	1	54	1	32.3	1.1	58.8	2.8	...	
0643−3314	06 43 34.55 −33 14 30.4	PKS 0641−331	238	239	212	181	5	68	5	87	4	220.8	6.6	296.1	9.2	...	
1109−3732	11 09 57.71 −37 32 20.0	NGC 3557	<118	<88	83	52	4	23	2	77	2	366.4	11.0	567.4	17.2	0.0102	G
1132−3227	11 32 27.53 −32 27 14.1	...	65	68	97	85	3	106	3	87	2	65.2	2.0	67.5	2.8	...	
1711−4552*	17 11 05.99 −45 52 54.1	...	<115	46	93	72	4	67	2	91	2	...	..	65.5	2.6	...	
1742−3435*	17 42 20.69 −34 35 15.2	...	81	95	144	136	7	..	..	..	..	21.9	0.9	22.2	1.7	...	
1745−4605*	17 45 35.32 −46 05 24.0	IC 1266	<101	<83	102	68	4	56	2	65	2	...	..	113.9	4.0	0.000	PN
1913−3630	19 13 21.03 −36 30 19.7	PMNJ 1913−3630	98	104	119	166	13	..	..	..	..	105.8	3.2	119.8	43.8	...	
1937−3958C	19 37 16.22 −39 58 01.6	PKS 1933−40	1199	1291	1669	1759	45	..	..	..	..	953.4	28.6	937.1	28.2	0.975	Q
1956−3225C	19 56 59.57 −32 25 45.1	PKS 1953−325	550	643	1000	709	51	..	..	..	..	473.6	14.2	474.1	14.4	1.242	Q
2000−4749	20 00 12.98 −47 49 51.7	...	<83	<85	73	79	4	..	..	..	..	...	..	7.4	1.0	...	
2003−4336	20 03 13.24 −43 36 33.1	PMNJ 2003−4336	<131	55	96	77	4	..	..	..	..	...	..	59.8	2.0	...	
2025−3931	20 25 42.54 −39 31 40.3	PMNJ 2025−3931	<118	<100	52	68	3	..	..	..	..	52.2	1.6	67.6	2.3	...	
2031−3647	20 31 49.14 −36 47 42.1	...	<108	<75	70	62	3	..	..	..	..	33.2	1.1	28.6	1.5	1.5683	Q
2039−5001	20 39 48.79 −50 01 12.1	MRC 2036−501	92	89	102	105	5	..	..	..	..	...	..	524.6	19.7	...	G
2056−4714C	20 56 16.42 −47 14 48.1	WMAP 208	1143	1086	1993	1711	55	..	..	..	..	...	..	2138.0	64.2	1.489	Q
2223−3137	22 23 21.69 −31 37 03.0	PKS 2220−318	485	476	642	..	..	447	10	329	6	220.7	6.6	274.7	8.4	...	Q?
2235−4835C	22 35 13.27 −48 35 58.8	WMAP 206	2605	...	...	1994	75	2065	518	1207	35	...	..	1216.0	36.5	0.510	Q
2235−3629	22 35 54.86 −36 29 02.1	...	268	272	246	..	..	156	39	120	4	68.2	2.1	74.4	2.7	...	
2245−4931	22 45 00.24 −49 31 48.2	PKS 2242−498	<114	<81	84	97	4	51	23	88	3	...	..	310.3	9.4	...	
2248−3235C	22 48 38.81 −32 35 50.8	PKS 2245−328	1166	1170	1655	..	..	826	207	410	12	708.0	21.2	710.5	21.4	2.268	Q
(c) Strong sources from the ATCA calibrator list																	
0004−4736C	00 04 35.65 −47 36 19.2	PKS 0002−478	893	...	...	868	16	970	59	900	30	...	..	932.9	28.0	...	
0012−3954C	00 12 59.89 −39 54 26.4	WMAP 202	734	716	1420	1609	33	2009	121	2015	67	465.0	14.0	839.9	25.3	...	
0051−4226C	00 51 09.50 −42 26 32.6	PKS 0048−427	708	...	...	1462	32	1544	93	1267	42	...	..	689.8	20.8	1.749	Q
0440−4333C	04 40 17.16 −43 33 08.4	WMAP 147	460	439	1533	1947	51	2961	74	3681	28	...	..	5858.0	175.8	2.863	Q
0631−4154C	06 31 12.00 −41 54 27.1	PKS 0629−418	165	162	399	517	17	623	35	708	40	...	..	684.9	20.6	1.416	Q
0648−3044C	06 48 14.17 −30 44 19.2	PKS 0646−306	780	851	929	744	24	713	40	772	43	1295.2	1.0	985.3	29.7	0.455	Q
1107−4449C	11 07 08.58 −44 49 06.8	WMAP 166	645	...	...	1674	40	2174	59	2703	50	...	..	2516.0	75.5	1.598	Q
1454−4012C	14 54 33.19 −40 12 31.5	PKS 1451−400	222	246	462	526	15	571	16	719	16	960.9	28.8	1210.0	36.3	1.810	Q
2158−3013C	21 58 51.93 −30 13 31.0	PKS 2155−304	310	327	388	350	10	377	21	369	10	424.2	12.7	479.2	14.6	0.116	Q

Table 5. Table of 2006 observations. 'C' after the source name in the first column indicates an ATCA calibrator.

Name	Radio position (J2000)	Alternate name	B_J	T	2006 S_{95} mJy	2006 S_{20} mJy	2004 S_{20} mJy	±	2004 $S_{8.6}$ mJy	±	2004 $S_{4.8}$ mJy	±	NVSS $S_{1.4}$ mJy	±	SUMSS S_{843} mJy	±	z	ID
0006−4245	00 06 19.72 −42 45 18.3	PKS 0003−430	18.27	2	55	148	183	4	189	11	199	7	...	..	246.0	7.7	1.780	Q
0012−3954C	00 12 59.89 −39 54 26.4	WMAP 202	18.33	2	496	984	1609	33	2009	121	2015	67	493.6	17.4	839.9	25.3	...	
0024−4202C	00 24 42.95 −42 02 03.5	PKS 0022−423	22.78	2	45	267	287	7	992	60	1956	65	...	..	1770.0	53.1	0.937	Q
0030−4224	00 30 17.51 −42 24 46.3	PKS 0027−426	18.15	2	274	389	478	10	511	31	511	17	...	..	424.8	12.8	0.495	Q
0040−3243	00 40 17.63 −32 43 27.6	PMNJ 0040−3243	21.59	2	128	285	314	5	276	17	231	8	210.7	6.3	178.2	5.6	...	
0040−3225	00 40 30.73 −32 25 19.9	PKS 0038−326	21.41	2	89	167	193	4	200	12	194	7	111.4	3.4	138.1	4.5	...	Q
0058−3234	00 58 02.22 −32 34 20.5	PKS 0055−328	20.03	2	140	198	327	6	309	19	265	10	185.9	5.6	184.1	5.8	...	
0058−3347	00 58 15.70 −33 47 57.1	PMNJ 0058−3347	20.54	2	103	139	174	4	217	13	214	7	129.2	3.9	118.4	3.8	...	
0106−4034C	01 06 45.11 −40 34 19.5	WMAP 171	18.60	2	2199	4160	2146	79	1549	38	1099	77	...	..	650.9	19.6	0.584	Q
0118−4102	01 18 45.27 −41 02 30.6	PKS 0116−413	19.44	2	82	186	172	6	211	5	228	19	...	..	1020.4	30.7	...	
0133−4430	01 33 00.87 −44 30 43.3	PKS 0130−447	>22	0	81	205	215	8	295	8	422	31	...	..	455.1	13.8	...	
0134−3843C	01 34 32.14 −38 43 33.7	MRC 0132−389	17.76	2	645	809	685	23	507	12	438	31	569.1	17.1	659.9	19.8	2.140	Q
0136−4044	01 36 02.88 −40 44 50.4	PMNJ 0136−4044	21.36	2	190	274	350	11	273	7	226	16	...	..	115.1	3.6	0.649	Q
0144−3938	01 44 54.10 −39 38 10.8	PMNJ 0144−3937	21.85	2	78	133	200	7	228	6	229	16	89.4	2.7	82.2	2.7	...	
0155−4048C	01 55 37.07 −40 48 42.4	PKS 0153−410	19.31	1	125	405	426	14	800	20	1252	88	...	..	2426.0	72.8	0.226	G
0157−3829	01 57 19.72 −38 29 44.4	.....	20.41	2	86	154	232	8	159	4	91	7	29.2	1.0	27.6	1.7	...	
0206−3024	02 06 43.28 −30 24 58.4	PKS 0204−306	22.62	2	55	161	180	6	342	4	499	7	844.3	25.3	987.1	29.7	...	G
0216−3247	02 16 48.19 −32 47 40.6	PKS 0214−330	18.88	2	270	455	540	15	504	5	330	5	165.2	5.0	152.1	4.9	1.331	Q
0227−3026	02 27 40.55 −30 26 04.2	PKS 0225−306	18.79	2	308	204	452	13	355	4	310	4	293.6	8.8	251.9	8.1	0.303	Q
0231−4746	02 31 11.77 −47 46 12.0	PMNJ 0231−4746	17.87	2	418	834	775	19	555	6	363	5	...	..	42.8	1.6	...	
0238−3031	02 38 55.31 −30 32 02.6	PMNJ 0238−3032	18.20	2	196	220	173	5	185	2	186	3	165.4	5.9	210.5	6.5	...	
0245−4459	02 45 54.07 −44 59 39.5	PKS 0244−452	17.65	1	287	420	581	17	591	6	688	9	...	..	1972.0	59.2	0.280	Q
0246−4651	02 46 00.09 −46 51 16.8	PKS 0244−470	18.40	2	218	353	397	12	516	5	677	9	...	..	1520.0	45.6	...	
0300−4959	03 00 27.80 −49 59 11.8	...	>22	0	<108	141	170	6	214	8	171	3	...	..	300.7	9.1	...	
0317−4414	03 17 57.66 −44 14 16.9	ESO 248−G006	15.74	1	112	377	258	9	449	17	611	8	...	..	1915.0	57.5	0.0761	G
0320−3837	03 20 46.43 −38 37 28.4	PKS 0318−388	—	–	138	162	161	5	145	6	135	2	175.2	5.3	205.5	6.3	...	
0330−4014	03 30 51.11 −40 14 16.3	PKS 0329−404	22.40	2	186	326	311	10	470	18	577	8	...	..	938.4	28.2	...	
0332−4455	03 32 44.10 −44 55 57.1	PKS 0330−450	17.69	2	66	195	180	6	227	9	159	2	...	..	111.4	3.5	2.60	Q
0334−4008C	03 34 13.62 −40 08 25.3	WMAP 146	17.51	2	353	552	1274	42	1124	43	943	13	...	..	986.5	29.7	...	Q
0334−3725	03 34 15.49 −37 25 43.2	PMNJ 0334−3725	17.08	2	322	358	293	10	319	12	313	4	221.2	7.8	171.4	5.3	...	
0336−3616	03 36 54.11 −36 16 06.0	PKS 0335−364	18.40	2	640	805	738	22	610	23	496	7	500.9	15.0	526.2	15.9	1.541	Q
0342−3703	03 42 05.41 −37 03 21.0	PKS 0340−37	17.85	2	59	236	217	7	324	13	696	9	2059.6	72.6	3126.0	93.8	0.284	Q
0402−3147C	04 02 21.31 −31 47 25.7	PKS 0400−319	20.33	2	308	536	467	9	587	15	632	5	681.3	20.4	506.5	15.3	1.288	Q
0407−3303C	04 07 33.92 −33 03 45.3	PKS 0405−331	19.33	2	321	692	563	14	659	16	634	5	634.9	19.1	697.7	21.0	2.562	Q
0415−4637	04 15 58.69 −46 37 49.2	PKS 0414−467	21.75	1	80	198	171	5	287	7	358	3	...	..	477.9	14.4	...	

Table 5 – *continued*

Name	Radio position (J2000)	Alternate name B_J	T	S_{95}	2006 S_{20} mJy	2006 S_{20} mJy	± mJy	2004 $S_{8.6}$	± mJy	2004 $S_{4.8}$	± mJy	2004 $S_{1.4}$	NVSS ± mJy	S_{843}	SUMSS ± mJy	z	ID	
0421−4818	04 21 27.49 −48 18 05.3	PKS 0419−484	16.85	2	212	321	452	13	356	9	232	2	...	..	284.8	8.6	0.527	Q
0422−3315	04 22 54.29 −33 15 08.7	PKS 0421−333	21.72	2	93	171	179	5	286	7	427	3	950.5	28.5	1347.0	40.5	...	
0439−4522C	04 39 00.83 −45 22 22.6	PKS 0437−454	20.45	2	266	442	700	17	890	22	928	7	...	..	950.9	28.6	...	
0441−3340C	04 41 33.67 −33 40 03.7	PKS 0439−337	22.48	1	<107	238	269	7	541	14	799	6	1155.9	34.7	896.0	27.0	...	
0441−3300	04 41 34.97 −33 00 08.1	PKS 0439−331	19.86	2	83	167	160	4	175	4	186	2	140.9	4.3	233.0	7.3	...	
0449−4809	04 49 39.59 −48 09 40.9	PMNJ 0449-4809	18.54	2	80	284	209	6	261	7	221	2	...	..	99.9	3.1	...	
2003−3251C	20 03 24.04 −32 51 42.5	PKS 2000−330	18.83	2	61	401	504	22	...	..	...	..	446.0	15.7	300.8	9.2	3.773	Q
2006−3451	20 06 46.31 −34 51 14.6	PMNJ 2006−3450	20.53	2	86	169	177	8	...	..	...	..	96.0	2.9	108.8	3.5	...	
2009−4849C	20 09 25.45 −48 49 53.9	PKS 2005−489	15.75	1	521	737	877	42	...	..	...	..	...	..	1299.0	39.0	0.071	G
2012−4721	20 12 09.52 −47 21 20.2	PMNJ 2012−4721	20.74	1	52	138	175	8	...	..	...	..	...	..	298.9	9.0	...	
2024−3253	20 24 35.69 −32 53 36.8	PKS 2021−330	18.73	2	272	438	479	23	...	..	...	..	886.5	26.6	1201.0	36.1	1.471	Q
2027−4726	20 27 50.74 −47 26 20.3	PMNJ 2027−4726	21.75	1	160	254	305	15	...	..	...	..	...	..	230.5	7.0	...	
2056−4714C	20 56 16.39 −47 14 48.1	WMAP 208	18.29	2	2453	3246	1711	55	...	..	...	..	...	..	2138.0	64.2	1.489	Q
2105−4848	21 05 01.20 −48 48 46.8	PKS 2101−49	17.31	2	173	516	468	14	687	39	735	20	...	..	1516.0	45.5	...	
2108−4846C	21 08 50.80 −48 46 21.8	PKS 2105−48	20.03	2	78	212	225	7	420	24	586	16	...	..	1459.0	43.8	...	
2123−3046	21 23 48.69 −30 46 06.2	PMNJ 2123−3046	19.18	2	57	293	179	6	271	15	300	8	147.2	4.4	155.8	5.1	...	
2124−4948	21 24 29.12 −49 48 06.8	PMNJ 2124−4948	19.46	2	<92	74	171	6	210	12	211	6	...	..	222.3	6.8	...	
2145−3142	21 45 47.01 −31 42 34.0	PKS 2142−319	20.82	2	129	152	165	6	184	11	169	5	144.3	4.4	188.1	5.9	0.66	Q
2151−3027C	21 51 55.58 −30 27 53.8	PKS 2149−306	17.95	2	849	1402	1846	58	1314	73	1302	36	1243.2	37.3	1088.0	32.7	2.345	Q
2158−3013C	21 58 52.08 −30 13 32.4	PKS 2155−304	12.35	2	903	844	350	10	377	21	369	10	489.3	19.0	479.2	14.6	0.116	Q
2229−4051C	22 29 18.61 −40 51 32.5	PKS 2226−41	19.58	2	49	277	254	10	790	198	1128	33	...	..	4230.0	129.6	0.4462	Q
2230−4416	22 30 56.44 −44 16 30.0	PKS 2227-445	19.46	2	350	472	472	18	628	157	423	12	...	..	520.1	15.7	1.326	Q
2235−4835C	22 35 13.29 −48 35 58.7	WMAP 206	17.61	2	1076	1775	1994	75	2065	518	1207	35	...	..	1216.0	36.5	0.510	Q
2257−3627C	22 57 10.60 −36 27 44.0	IC 1459	11.49	1	264	621	...	..	1208	303	1198	35	1279.7	45.2	966.2	29.1	0.0056	G
2300−3536	23 00 55.92 −35 36 15.9	PMNJ 2300−3536	21.08	2	97	174	220	3	220	9	161	3	97.9	3.0	88.8	3.1	...	
2302−3718	23 02 23.77 −37 18 07.3	PKS 2259−37	>22	0	41	240	261	4	585	24	986	13	2719.8	81.6	4243.0	127.3	...	
2302−4533C	23 02 40.04 −45 33 57.7	PKS 2259−458	20.46	1	93	148	165	3	194	4	305	4	...	..	1059.3	31.8	...	
2307−3548	23 07 37.27 −35 48 28.7	...	21.14	1	106	118	190	3	186	8	112	2	58.7	2.2	93.5	3.1	...	
2308−4557	23 08 52.81 −45 57 56.1	...	19.39	1	199	225	286	4	212	9	163	2	...	..	214.3	6.5	...	G
2313−4729C	23 13 51.91 −47 29 11.7	PKS 2311−477	22.20	1	53	181	189	3	421	18	647	9	...	..	966.5	29.0	...	
2314−4455C	23 14 09.38 −44 55 48.9	PKS 2311−452	19.95	2	125	439	497	7	981	41	1391	19	...	..	2863.0	85.9	2.884	Q
2316−4337C	23 16 21.07 −43 37 47.0	PKS 2313−439	19.82	2	124	303	319	5	523	22	682	9	...	..	1384.0	41.6	1.847	Q
2316−4041	23 16 46.90 −40 41 20.7	PKS 2314−409	18.76	2	82	247	245	4	392	16	397	5	...	..	520.8	15.8	2.448	Q
2318−4010	23 18 06.88 −40 10 06.5	PKS 2315−404	19.52	2	157	231	188	3	235	10	288	4	...	..	296.8	9.1	1.820	Q
2318−4032	23 18 09.29 −40 32 06.7	PKS 2315−408	18.97	2	52	166	173	3	333	14	502	7	...	..	1329.0	39.9	...	

(vi) Simultaneous ATCA 95- and 20-GHz flux densities measured in 2005–6 in this project.

(vii) Near-simultaneous ATCA 20-, 8- and 5-GHz flux densities measured by the AT20G team in 2004 November. The listed values are from the 2007 July run of the AT20G data pipeline.

(viii) Lower-frequency flux density measurements from the 1.4-GHz NVSS (Condon et al. 1998) and 843-MHz SUMSS (Mauch et al. 2003) catalogues. The SUMSS values are taken from v2.0 of the catalogue (released on 2007 August).

(ix) The spectroscopic redshift of the optical counterpart, where this is available either from the NASA/IPAC Extragalactic Data base (NED) or from the 6dFGS Third Data Release (Jones et al., in preparation).

(x) NED classification as QSO (Q) or galaxy (G), where available. These classifications are taken from papers in the literature and usually (but not always) agree with the Supercosmos classification.

Appendix A contains some notes on the properties of individual sources.

4 DATA ANALYSIS

4.1 Stability of the 95-GHz flux density measurements

A comparison of the 95-GHz flux densities measured on the first and second days of our 2005 run is shown in Fig. 3. The flux densities measured on the two days agree to within 10 per cent (i.e. within the quoted error bars from Table 3), even though conditions on the first day were cloudy with poor phase stability. We therefore conclude that our techniques for measuring 95-GHz flux densities yield results which are stable and reproducible. This is important, because we are measuring continuum sources which are significantly weaker than have previously been observed with the ATCA in the 95-GHz band.

4.2 The inverted-spectrum and flux-limited samples

As noted in Table 2, our 2005 observations included 59 inverted-spectrum sources which were selected to have rising radio spectral index ($\alpha > 0$) between 8 and 20 GHz. The sample selection was done in 2005 July, using preliminary flux density measurements from a reduction of the AT20G data carried out in late 2004.

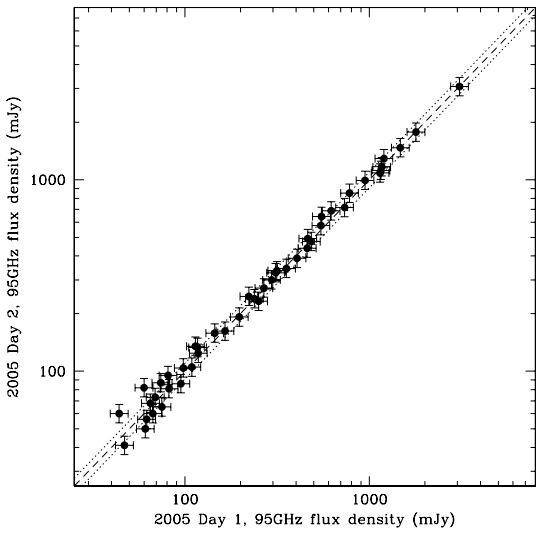

Figure 3. Comparison of two independent 95-GHz measurements (taken one day apart) of AT20G sources observed in our 2005 July run. The dotted lines show a 10 per cent deviation from equality.

After our 2005 observations were completed, the AT20G team implemented a new data pipeline which included an improved calibration process and a stringent set of checks designed to identify poor-quality data. As a result of these checks, 13 galaxies in our 2005 sample (all in the RA range $17^{\rm h}$–$22^{\rm h}$) had their 8- or 20-GHz AT20G flux measurements flagged as unreliable. Since we could no longer be sure that these sources qualified as 'inverted spectrum', they were not included in our analysis. Two other sources no longer had rising 8–20 GHz spectra after recalibration, and were also removed.

Finally, we tightened the selection criteria for the inverted spectrum sample to require that the sources had $\alpha > 0$ at 5–8 GHz as well as 8–20 GHz. The aim was to restrict the sample to objects whose radio spectra were genuinely inverted over the full 5–20 GHz AT20G frequency range, and to avoid contamination by sources whose spectra were flat ($\alpha \sim 0$) at 5–20 GHz but which happened to have a slightly higher flux measurement at 20 GHz than at 8 GHz. A further seven (mostly weak) sources were removed by this test.

All 59 sources observed in 2005 are listed in Table 4, with the 39 sources included in our final inverted-spectrum analysis clearly identified.

Table 5 lists the 70 sources in our 2006 'flux-limited' sample, which were selected to have 20-GHz flux densities above 150 mJy. One object (2257−3627, the nearby galaxy IC 1459) later had its 2004 AT20G flux density at 20 GHz flagged as unreliable. Although it is listed in Table 5, it was not included in our analysis. Our final flux-limited sample therefore contains 69 objects.

4.3 Variability at 20 and 95 GHz

Sadler et al. (2006) examined the variability of a flux-limited ($S_{20} > 100$ mJy) sample of 108 AT20G sources by comparing measurements from 2003 and 2004. They found that the general level of variability at 20 GHz was quite low, with a median variability index for their sources of 6.9 per cent. Only five sources varied by more than 30 per cent over the one-year interval.

We can also use the 2004 AT20G measurements as a benchmark to measure the variability of the sources in Tables 4 and 5 at 20 GHz. To do this, we calculated a debiased variability index for each object as described in section 6 of Sadler et al. (2006). The results are summarized in Table 7. For both the 'inverted-spectrum' sample observed in 2005 (Table 4) and the flux-limited sample observed in 2006 (Table 5), the median variability index at 20 GHz is close to that found by Sadler et al. (2006) for their flux-limited source sample.

In contrast to the results at 20 GHz, we have very little data so far on variability at 95 GHz. There are only eight sources in common between our 2005 and 2006 data sets (see Table 6), and these turn out by chance to be drawn mainly from the more variable objects in their parent samples. Any results based on this small sample are no more than suggestive, but we see no evidence at this stage that our sources are more variable at 95 GHz than at 20 GHz (see Table 7). The spectral index values in Table 6 also suggest that the measured 20–95 GHz spectral index may not change significantly when a source varies in flux density at these frequencies, though the size of the error bars makes it difficult to draw any strong conclusion from a sample of only seven repeat observations.

Table 6. Flux density and spectral-index measurements for the eight sources from Tables 4 and 5 which were observed in both the 2005 and 2006 runs. 2235−4835 was not observed at 20 GHz in 2005.

Name	—— S20 (mJy) ——				— S95 (mJy) —				—— Spectral index α_{95}^{20} ——			
	2004	±	2005	±	2006	±	2005	±	2006	±	2005	±	2006	±
0013−3954	1609	33	1420	77	984	105	716	84	496	51	−0.44	0.12	−0.44	0.14
0106−4034	2146	79	2632	142	4160	445	1775	209	2199	224	−0.25	0.12	−0.41	0.14
0136−4044	350	11	380	21	274	29	344	41	190	19	−0.06	0.12	−0.23	0.14
0421−4817	452	13	513	28	321	34	300	35	212	22	−0.34	0.12	−0.27	0.14
2056−4714	1711	55	1993	108	3246	347	1086	128	2453	250	−0.39	0.12	−0.18	0.14
2151−3027	1846	58	2108	114	1402	150	688	81	849	87	−0.72	0.12	−0.32	0.14
2158−3013	350	10	388	21	844	90	327	39	903	92	−0.11	0.12	+0.04	0.14
2235−4835	1994	75	...	..	1775	190	2605	307	1076	110	...	..	−0.32	0.14

Table 7. Median variability index at 20 and 95 GHz for several sets of data observed with the ATCA. The AT20G pilot results for 2003–4 are taken from Sadler et al. (2006). The small sample of 'repeat' sources which we observed in both 2005 and 2006 have a significantly higher median variability index than either of the parent samples from which they came.

Data set	Frequency (GHz)	Time interval	N	Median variability index (per cent)
AT20G Pilot	20	2003–2004	108	6.9
Inverted spectrum	20	2004–2005	37	6.4
Flux limited	20	2004–2006	69	6.9
05–06 repeats	20	2004–2006	8	20.1
05–06 repeats	20	2005–2006	7	20.3
05–06 repeats	95	2005–2006	8	20.2

4.4 Comparison with the *WMAP* three-year source catalogue

Hinshaw et al. (2007) have recently released a catalogue of 323 radio sources detected by the *WMAP* satellite (Bennett et al. 2003) in five frequency bands at 23, 33, 41, 61 and 94 GHz. The *WMAP* catalogue identifies bright sources independent of their presence in other surveys at lower frequency. When a source is identified with $>5\sigma$ confidence in any of the five bands, the flux densities in other bands are also listed if they are $>2\sigma$. Only 121 of the 323 catalogued *WMAP* sources have flux densities listed at 94 GHz, and almost all of these are 23-GHz detections.

Table 8 lists the 13 sources in Tables 4 and 5 which were also detected by *WMAP* at 94 GHz. These objects are also plotted in Fig. 4. The mean flux density ratio ($S_{\rm ATCA}/S_{\rm WMAP}$) for the objects in Table 8 is 1.18 ± 0.14 at 20/23 GHz and 1.16 ± 0.06 at 95/94 GHz. Although the comparison sample is small and the sources were measured at different epochs, the results strongly suggest that the ATCA and *WMAP* data are on a common flux density scale to within about 15 per cent at 95 GHz. This also appears to confirm that our 95-GHz ATCA flux measurements have not been strongly affected by pointing and tracking effects (see Section 2.3.2).

4.5 The 20–95 GHz spectral-index distribution

As a first step in investigating the high-frequency properties of our sample, we calculated the two-point radio spectral index α_{20}^{95} for each of the objects in Tables 4 and 5. For the small number of 20-GHz sources which were undetected at 95 GHz, we used the upper limits in flux density to calculate a limiting value of α. Fig. 5 shows the distribution of α_{20}^{95} for the two samples. Only two sources in the flux-limited sample (0227−3026 and 2158−3013) show a rising spectrum from 20 to 95 GHz. Even in the inverted-spectrum sample (all of which were selected to have $\alpha_8^{20} > 0$), only seven out of the 37 sources have $\alpha_{20}^{95} > 0$. This contrasts strongly with the spectral-index distribution of AT20G sources at 8–20 GHz, where 40 per cent have rising spectra with $\alpha_8^{20} > 0$ (Sadler et al. 2006). As discussed by Lowe et al. (2007), this may be a selection effect, since the number of rising-spectrum sources in a sample selected at frequency ν will

Table 8. Comparison of flux densities for sources in common with the *WMAP* three-year catalogue (Hinshaw et al. 2007). The *WMAP* data were taken over the period 2001 August to 2004 August inclusive and so pre-date the ATCA observations, which were made in 2004 October, 2005 July and 2006 September.

AT20G name	Alternate name	—— 2006 ——				—— 2005 ——				— 2004 —		—— WMAP ——			
		S_{95} Jy	±	S_{20} Jy	±	S_{95} Jy	±	S_{20} Jy	±	S_{20} Jy	±	S_{94} Jy	±	S_{23} Jy	±
0012−3954	WMAP 202	0.50	0.05	0.98	0.10	0.72	0.08	1.42	0.08	1.61	0.03	...	...	1.4	0.06
0026−3512	PMNJ0026−3512	...	...	...	...	1.12	0.13	1.27	0.07	1.12	0.02	...	...	1.0	0.08
0106−4034	WMAP 171	2.20	0.22	4.16	0.45	1.78	0.21	2.63	0.14	2.15	0.08	1.3	0.3	1.8	0.05
0334−4008	WMAP 146	0.35	0.04	0.55	0.06	...	...	...	...	1.27	0.04	...	...	1.6	0.06
0440−4333	WMAP 147	...	...	...	...	0.44	0.04	1.53	0.16	1.95	0.05	...	...	3.0	0.07
0455−4615	WMAP 151	...	...	...	...	3.07	0.36	4.42	0.24	4.16	0.12	1.8	0.4	3.7	0.06
0538−4405	WMAP 148	...	...	...	...	8.08	0.95	7.33	0.40	5.29	0.22	4.6	0.4	5.4	0.06
1102−4404	PKS1059−438	...	...	...	...	0.49	0.06	0.49	0.03	0.77	0.02	...	...	0.6	0.05
1107−4449	WMAP 166	...	...	...	...	0.65	0.08	...	...	1.67	0.04	1.0	0.4	1.6	0.05
1427−3305	WMAP 193	...	...	...	...	1.47	0.17	0.87	0.05	0.77	0.02	...	...	3.2	0.07
1937−3958	PKS1933−40	...	...	...	...	1.29	0.15	1.67	0.09	1.76	0.05	...	...	0.7	0.08
2056−4714	WMAP 208	2.45	0.25	3.25	0.35	1.09	0.13	1.99	0.11	1.71	0.06	2.4	0.9	1.7	0.06
2235−4835	WMAP 206	1.08	0.11	1.78	0.19	2.61	0.31	...	...	1.99	0.08	2.1	0.5	1.7	0.06

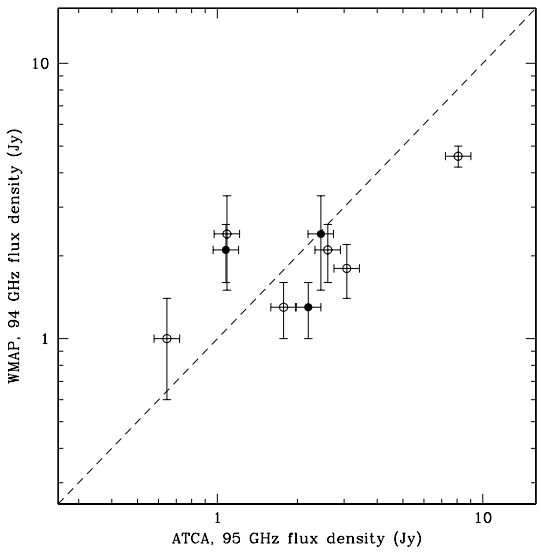

Figure 4. Comparison of our measured ATCA 95-GHz flux densities with those listed in the *WMAP* 3-yr source catalogue (Hinshaw et al. 2007) for sources in common (see also Table 8). The filled and open circles show data from the 2005 and 2006 ATCA runs, respectively.

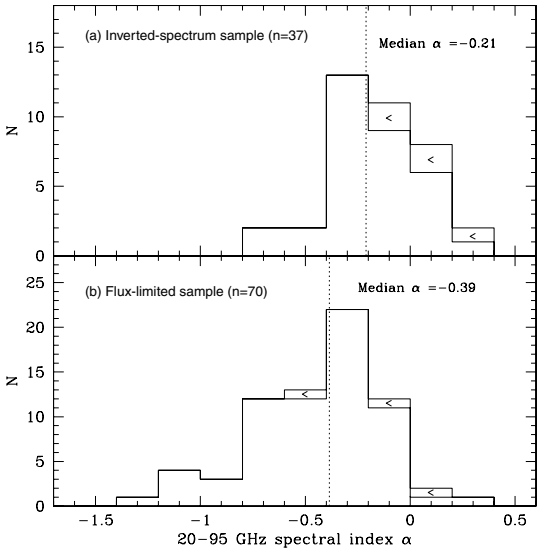

Figure 5. Histogram of 20–95 GHz spectral index α for (a) the inverted-spectrum sample observed in 2005 and (b) the flux-limited sample observed in 2006.

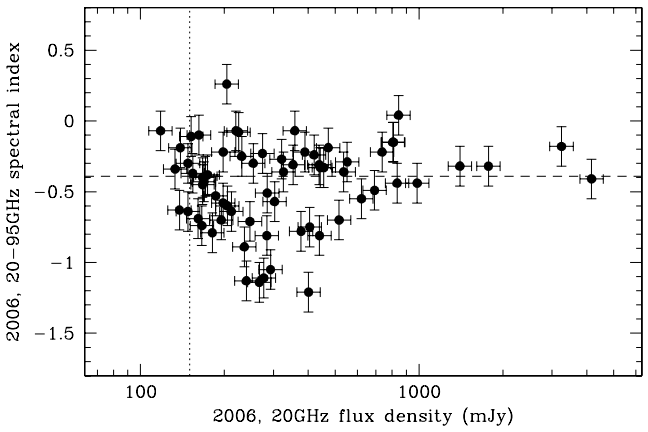

Figure 6. Plot of 20–95 GHz spectral index α_{20}^{95} against 20-GHz flux density for the flux-limited sample of sources in Table 4. The horizontal dashed line shows the median spectral index of −0.39, while the vertical dotted line shows the flux limit of 150 mJy used to select the sample. A few sources lie to the left-hand side of this line, because their 20-GHz flux density has decreased since the AT20G observations were made in 2004.

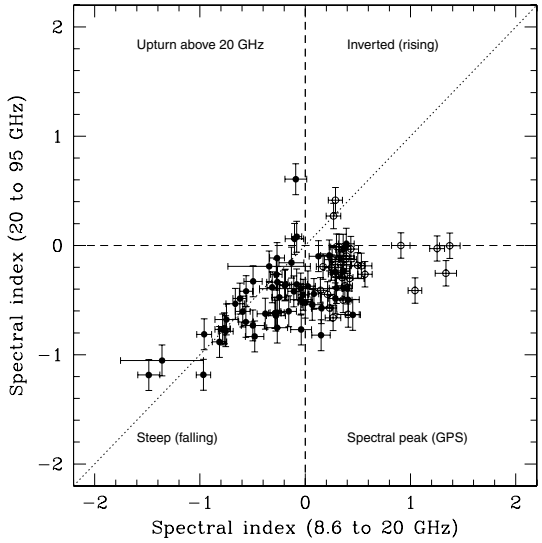

Figure 7. Two-colour radio spectral-index plot for the flux-limited (filled circles) and inverted-spectrum (open circles) AT20G samples. Only three sources still have a rising spectrum from 20 to 95 GHz, and almost all the sources with inverted spectra at 8–20 GHz have peaked and turned over by 95 GHz.

usually be greater when the spectral index is measured between ν and a lower frequency ν_1 than when it is measured between ν and a higher frequency ν_2.

The median 20–95 GHz spectral index for sources in our flux-limited sample is −0.39 and, as can be seen from Fig. 6, this does not change significantly with 20-GHz flux density over the range probed by our ATCA observations ($S_{20} > 150$ mJy). As we will show in Section 5, this allows us to use the 20-GHz extragalactic source counts measured from the AT20G survey, together with the observed distribution of α_{20}^{95}, to derive the overall radio source counts at 95 GHz.

We note that our median 20–95 GHz spectral index of −0.39 is much flatter than the value of −0.89 measured at 15–43 GHz by Waldram et al. (2007). The Waldram et al. (2007) sources are much fainter than those in our sample, since most of them have 22-GHz flux densities below the AT20G survey limit of 40 mJy. The work of Waldram et al. (2007) is therefore complementary to our study, and suggests that the 20–95 GHz spectral-index distribution of AT20G sources may steepen significantly at flux densities below 50–100 mJy.

4.6 Properties of the 5–95 GHz radio spectra

For the sources in this study, we have near-simultaneous data at 5, 8 and 20 GHz from the AT20G survey as well as simultaneous data (at a different epoch) at 20 and 95 GHz from our own ATCA observations. The mean and median values of the spectral index in each frequency interval are listed in Table 9. Both samples show a general steepening of the radio spectrum with increasing frequency. A

Table 9. Mean and median values of the radio spectral-index distribution for our 2006 flux-limited sample calculated for different frequency ranges. The three sources undetected at 95 GHz have been removed from the calculation of the mean value at 20–95 GHz.

Frequency (GHz)	Median α	Mean α	$\pm$	n	Notes
5–8	−0.11	−0.17	0.06	62	This paper
8–20	−0.24	−0.25	0.05	62	This paper
20–95	−0.39	−0.45	0.04	69	This paper

similar effect has been noted by Waldram et al. (2007) and Massardi et al. (2008).

Fig. 7 shows a radio two-colour diagram comparing the 8–20 and 20–95 GHz spectral indices. As discussed by Sadler et al. (2006), this diagram provides a useful way of classifying objects which (like many of the AT20G sources) have curved, rather than power-law radio spectra. The diagonal dotted line in Fig. 7 shows the power-law relation. As noted earlier, inverted-spectrum objects (which account for 18 per cent of all AT20G sources at 8–20 GHz) are almost absent (<2 per cent) at 20–95 GHz.

4.7 Optical properties of the 95-GHz sources

We used the Supercosmos catalogue (Hambly et al. 2001) to obtain optical identifications for the radio sources observed in this study. We accepted an optical object as the correct ID if it was brighter than $B_J = 22$ mag and lays within 2.5 arcsec of the radio position, since Monte Carlo tests imply that at least 97 per cent of such objects are likely to be genuine associations (Sadler et al. 2006). Optical identifications were not attempted for three sources within 10° of the Galactic plane, and one source in the flux-limted sample (0320−3837) was so close to a bright foreground star that no optical identification was possible.

Table 10 summarizes the optical properties of the two samples. While QSOs make up the majority of the optical IDs in both samples, the inverted-spectrum sample has a slightly higher fraction of galaxies and a median value of $B_J = 0.4$ mag fainter than the flux-limited sample.

Published redshifts are available for fewer than half the optical IDs, so the redshift distribution needs to be interpreted with caution. However, the lower median redshift for the inverted-spectrum sample is consistent with it containing a higher fraction of galaxies (which generally lie at $z < 0.5$ if visible on DSS images) than the flux-limited sample.

4.8 A correlation between 95-GHz flux density and optical magnitude?

Owen & Mufson (1977) found a correlation between optical magnitude and millimetre (90-GHz) flux density for a sample of flat-spectrum QSOs, and noted that this was surprising because of the 20–25 yr interval between their 90-GHz measurements and the sky survey plates from which the optical magnitudes were measured. They showed that the correlation was significant at the 99 per cent level at 90 GHz, yet the 5-GHz flux densities of the same sources were uncorrelated with optical magnitude. They interpreted this as evidence that the sources were optically thin at millimetre wavelengths but optically thick at centimetre wavelengths, and that a correlation existed between the radiation mechanisms in the optical and millimetre regimes.

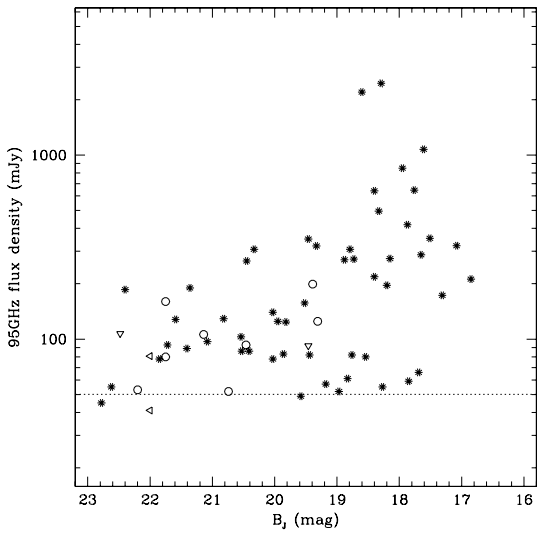

Figure 8. Plot of optical B_J magnitude from the SuperCOSMOS catalogue against 95-GHz flux density for objects in our flux-limited sample. Sources identified with QSOs are shown by the stars, and galaxies are shown by the open circles. Upper limits are indicated by the open triangles, and the horizontal line at 50 mJy shows the typical detection limit for our 2006 observations.

Fig. 8 shows a plot of 95-GHz flux density against optical B_J magnitude for our flux-limited sample, with separate symbols used for QSOs and galaxies. Blank fields are indicated by upper limits in B_J. We see a trend similar to that found by Owen & Mufson (1977), in the sense that brighter 95-GHz sources are associated with brighter optical objects. The correlation for QSOs in Fig. 8 is statistically significant at a level of >99.6 per cent in a rank correlation test.

One possible explanation is that many of the strongest 95-GHz sources are brightened by relativistic beaming at both optical and millimetre wavelengths, which would require that they are viewed at very small angles to the jet axis. In this orientation, the millimetre continuum emission can be Doppler-boosted by factors of up to 20 (Lähteenmäki & Valtaoja 1999) and the optical continuum brightened by at least one magnitude (Browne & Wright 1985).

In principle, optical spectroscopy can provide a test of the relativistic beaming model, since QSOs which are strongly beamed should have a lower line to continuum ratio than less beamed objects (Baker & Hunstead 1995). This would require a more complete and uniform set of optical spectra than is presently available for our sample.

Table 10. Optical properties of the two samples (excluding sources for which no optical ID was attempted). N_z is the number of sources in each sample which have a published optical redshift. Objects classed as 'Faint/blank' have optical IDs fainter than $B_J = 22.0$.

Sample	N	Gal	QSO	Faint/blank	Median B_J (mag)	N_z	Median z
Inverted spectrum	34	7 (21 ± 8 per cent)	23 (68 ± 14 per cent)	4 (11 ± 7 per cent)	19.84	12 (35 per cent)	0.56
Flux limited	69	11 (16 ± 5 per cent)	50 (73 ± 10 per cent)	8 (11 ± 4 per cent)	19.44	32 (46 per cent)	1.11

4.9 Sources with extended low-frequency radio emission

SUMSS images at 843 MHz are available for all our 95-GHz sources, and 1.4-GHz NVSS images for those north of declination -40°. The SUMSS and NVSS images have similar resolution (45 arcsec) and sensitivity (detection limits of a few mJy). Although all the sources in Tables 4 and 5 are unresolved at 20 and 95 GHz, several of them show extended emission on scales of 45–100 arcsec in the low-frequency SUMSS and NVSS images (see Appendix A). From the NVSS/SUMSS images alone, it is unclear whether the extended low-frequency emission arises only from the AT20G object, or includes a contribution from a nearby confusing source which is below the detection threshold at high frequencies.

Interestingly, all the sources with extended low-frequency emission are members of the inverted-spectrum sample. Five out of the 37 sources in the inverted-spectrum sample (14 per cent) have extended emission in the SUMSS images, whereas none of the 70 sources in the flux-limited sample does have. The reason for this difference is unclear at present. It may simply reflect the lower median redshift of the inverted-spectrum sample (see Table 10), but could also hint at genuine physical differences between the inverted-spectrum sources (and/or their environment) and the overall high-frequency radio population.

5 ATCA 95-GHz SOURCE COUNTS AND COMPARISON WITH EARLIER PREDICTIONS

As noted earlier, there are several reasons for wanting to measure the surface density of extragalactic radio sources at 95 GHz apart from the study of the intrinsic physical properties of these objects. In an ideal case, one would perform an all-sky survey at 90–100 GHz, but it is presently difficult to reach faint flux levels with such a survey. As noted in Section 1, the primary beam of most radio interferometers and single-dish telescopes operating at millimetre wavelength is tiny, making the mosaicking of any large area of sky an incredibly time-consuming task.[3] Additional challenges include the high system temperatures at 90–100 GHz and changing weather conditions which can make the sensitivity level of ground-based surveys uneven.

The *Planck* satellite scheduled for launch in 2008 will survey the whole sky with an estimated 5σ point-source detection limit of $\sim$500 mJy at 30 GHz and $\sim$280 mJy at 100 GHz (López-Caniego et al. 2006). These limits are set by confusion, and the rms noise per pixel is much lower (14 mJy at 100 GHz and 10.2 mJy at 143 GHz (Lamarre et al. 2003). As a result, there is a lot of astrophysical information in *Planck* maps below the confusion limit, and some of this can be extracted, for example, using stacking techniques, by making use of the AT20G survey and follow-up observations at higher frequencies.

Since a blind survey of the whole sky to low flux levels at frequencies above 20 GHz is presently impractical, we use a method first proposed by Kellermann (1964) to predict the extragalactic source counts at 95 GHz, based on our knowledge of the observed 20-GHz source counts from the AT20G survey and the observed 20–95 GHz spectral-index distribution presented in Section 4.5 of this paper.

[3] For example, a blind survey carried at 100 GHz with the same observational set-up used for the AT20G survey at 20 GHz (three baselines; 8-GHz analogue correlator and fast meridian scanning; see e.g. Sadler et al. 2006) on the same 1500-deg^2 sky strip explored by the AT20G Pilot Survey ($-70^\circ < \delta < -60^\circ$; see Ricci et al. 2004) would require a month of observing time at the ATCA instead of the five days needed at 20 GHz. With a detection limit of $\sim$300 mJy, this 100-GHz survey would detect less than one source a day.

5.1 Methodology

The technique developed by Kellermann (1964) is based on the idea that if one knows both the source counts at one frequency and the distribution of flux densities for a complete subsample at a second frequency, it is possible to predict the source counts at the second frequency.

The method makes no assumption about the actual spectral shape between the two frequencies, but it is convenient to characterize the flux ratio by the spectral index for an assumed power law. It does assume that the distribution of flux ratios (i.e. the spectral-index distribution) correctly characterizes all the source populations present. If the spectral-index distribution is a function of flux density, or if some class of sources becomes important at the second frequency but is not represented at the first frequency, the prediction will fail. For this reason it is important to start with reliable source counts at a frequency as close as possible to the second frequency.

The method we followed (outlined by Kellermann, Pauliny-Toth & Davis 1968) first assumes that the ratio of the flux densities S_1 and S_2 at two frequencies ν_1 and ν_2 is represented by the spectral index α defined as

$$S_2 = S_1 \times \left(\frac{\nu_2}{\nu_1}\right)^{\alpha}. \quad (1)$$

The observed spectral index distribution $P(\alpha)$ and the counts $n(S_1, \nu_1)$ at any given frequency ν_1 above the flux density limit S_1 can then be used to predict the source counts $n(S_2, \nu_2)$ at another frequency ν_2 above the flux density limit S_2 using the formula

$$n(S_2, \nu_2) = \int_{-\infty}^{+\infty} n\left[\left(\frac{\nu_2}{\nu_1}\right)^{-\alpha} S_2, \nu_1\right] P(\alpha)\,\mathrm{d}\alpha, \quad (2)$$

provided that the $P(\alpha)$ is independent of flux density.

For our flux-limited sample with $S_{20} > 150$ mJy and a median 20–95 GHz spectral index of -0.39, the equivalent flux density limit at 95 GHz is 82 mJy.

5.2 Completeness of the 95-GHz source populations

As noted above, the method we are using to predict the 95-GHz source counts will give unreliable results if any class of sources which is present at 95 GHz is not represented in our 20-GHz source counts.

In our case, any new population of sources appearing at 95 GHz would have to have a very rapidly rising spectrum between 20 and 95 GHz in order to be weaker than the AT20G detection limit of 40 mJy at 20 GHz. At the 1 Jy level at 95 GHz, this would require a population with a high-frequency radio spectral index $\alpha > +2.0$. Even at the 100-mJy level, a high-frequency spectral index $\alpha > +0.6$ would be required.

No sources with such extreme 20–95 GHz spectral indices are seen in our present 95-GHz data set, apart from a small population of optically thick thermal sources in our own Galaxy (which all lie at low Galactic latitude). As can be seen from Figs 5 and 7, almost all AT20G sources with $\alpha > 0$ at 8–20 GHz have lower flux densities at 95 GHz than at 20 GHz. Bolton et al. (2004) also found no sources with $\alpha > +0.6$ at 15–43 GHz in their sample of sources selected at 15 GHz, with flux densities as low as 25 mJy.

At this stage therefore we see no evidence that that our 20-GHz sample is missing any source population which contributes to the 95-GHz source counts at levels above about 100 mJy.

Table 11. Best-fitting parameters for the 20-GHz source counts measured from the AT20G survey at declination $-90^\circ < \delta < -15^\circ$ (Ricci et al., in preparation).

Parameter	Fitted value	Units
α	$1.92^{+0.03}_{-0.02}$	
β	$2.78^{+0.09}_{-0.07}$	
S_*	$1.09^{+0.13}_{-0.18}$	Jy
N_*	$28.9^{+13.7}_{-6.8}$	Jy sr^{-1}

Table 12. Parametrization of our predicted 95-GHz source counts plotted in Fig. 9. The fit was done in the same way as for the 20-GHz counts in Table 11.

Parameter	Fitted value	Units
α	1.92	
β	2.77	
S_*	0.80	Jy
N_*	19.45	Jy sr^{-1}

5.3 Differential radio-source counts at 95 GHz

Since the 20-GHz counts show some curvature, we made our final estimate by fitting the AT20G source counts with a double power law of the form:

$$N(S) = \frac{2N_*}{[(S/S_*)^\alpha + (S/S_*)^\beta]}, \quad (3)$$

where the best-fitting parameters for the two slopes α and β, the flux density of the break S_* and number count at the break N_* are given in Tables 11 and 12.

We then derived the differential source counts at 95 GHz using the methods outlined in Section 5.1. The results are shown in Figs 9 and 10, and are valid for flux densities above 80 mJy at 95 GHz.

5.4 Comparison with previously published values

Figs 9 and 10 also compare our 95-GHz differential source counts with previous predictions by Holdaway, Owen & Rupen (1994), De Zotti et al. (2005) and Waldram et al. (2007).

Holdaway et al. (1994) observed a sample of 367 flat-spectrum radio sources at 90 GHz with the NRAO 12-m telescope in 1993. Just under 80 per cent of their sample was detected above a 3σ limit of 90 mJy. Holdaway et al. (1994) then used VLA 8.4-GHz measurements of the same objects (Patnaik et al. 1992) to calculate the 8–90 GHz spectral index distribution for their sample, and combined this with the 5-GHz source counts measured by Condon (1984) to estimate the source counts at 90 GHz.

The 8- and 90-GHz observations were separated in time by almost four years (the data were taken in 1990 February and 1993 November, respectively), and so the measured 8–90 GHz spectral index distribution is likely to be broadened by source variability over the intervening period of almost four years. The Holdaway et al. (1994) analysis also depends critically on the assumed ratio of core to total flux density at 5 GHz, since the 5-GHz source counts measure total flux density but their 8–90 GHz data essentially measures the spectral index of a compact core.

Their predicted source counts from Holdaway et al. (1994) are valid for the flux density range $S_{90} > 0.1$ Jy, set by the detection limit of the high-frequency survey they used.

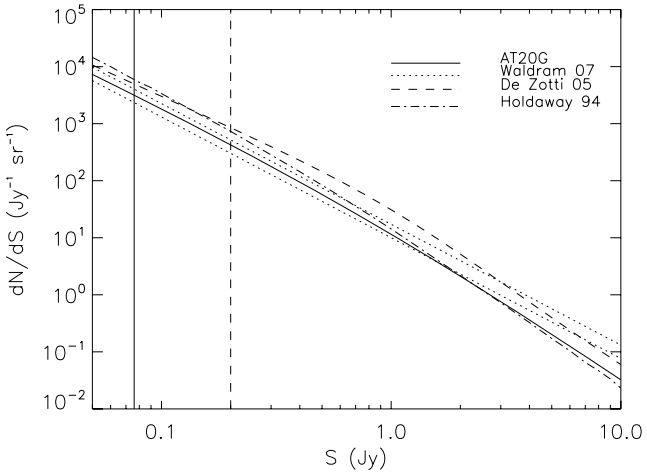

Figure 9. Differential source-count predictions from AT20G 20-GHz counts scaled to 95 GHz (this paper); De Zotti et al. (2005) model counts at 94 GHz; Waldram et al. (2007) at 94 GHz; and Holdaway et al. (1994) at 90 GHz. The vertical solid line represents the lower bound of validity for our counts (82 mJy), and the vertical dashed line is the upper bound of validity for the Waldram et al. counts (200 mJy).

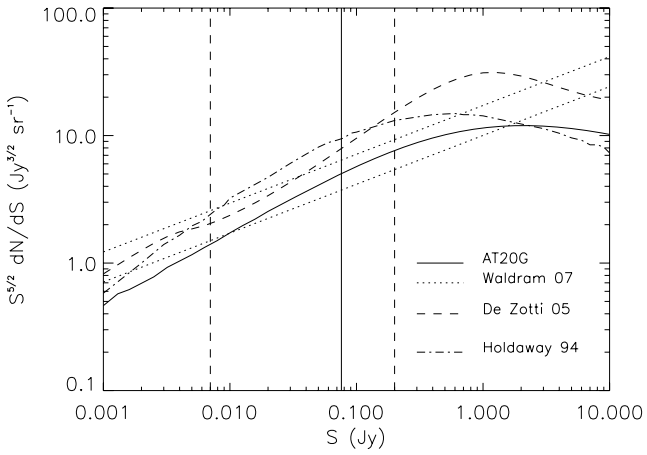

Figure 10. Differential 95-GHz source counts normalized to the Euclidean case for the same four estimates shown in Fig. 9. The flux density scale now extends down to 1 mJy. As before, the vertical solid line represents the lower bound of validity for our counts. The two vertical dashed lines show the lower and upper bounds of validity for the Waldram et al. (2007) predictions.

Radio source counts at 94 GHz have been estimated using the evolutionary models described by De Zotti et al. (2005), which take into account the epoch-dependent radio luminosity functions of the various source populations which contribute to the high-frequency counts. The 94-GHz counts are derived by making the additional assumption that all flat-spectrum sources have a simple power-law spectrum with $\alpha = -0.1$ above 20 GHz (De Zotti et al. 2005).

The De Zotti et al. (2005) model counts at 20 and 30 GHz are calculated over a wide range in flux density (0.01 mJy to 10 Jy), though De Zotti et al. (2005) note that there are large uncertainties below $\sim$0.1 mJy. Both Sunyaev–Zeldovich signals and free–free emission from protogalactic plasma are likely to contribute significantly at sub-mJy flux levels, but there are presently almost no observational data available to constrain the models.

Waldram et al. (2007) have recently estimated the source counts at 90 GHz based on the 15-GHz source counts from their 9C survey (Waldram et al. 2003) combined with follow-up 22- and 43-GHz VLA observations of a flux-limited sample of 121 sources selected at 15 GHz. The Waldram et al. (2007) source-count predictions are valid for the flux density range between 10 and 200 mJy, since their 15-GHz survey area contains very few strong sources.

Our derived 95-GHz source counts are in good agreement with the counts published by Waldram et al. (2007) in the flux density range where both data sets are valid (80–200 mJy; see Fig. 10). This is encouraging, as the two derivations are based on completely independent data sets.

In contrast, our 95-GHz counts are significantly lower than the values derived by Holdaway et al. (1994) for all but the brightest sources, and are also lower than the De Zotti values at all flux densities. In the case of the De Zotti counts, the discrepancy almost certainly arises, because De Zotti assumed a power-law spectral index of -0.1 at 20–94 GHz, whereas our 95-GHz data show that the median spectral index of AT20G sources in this frequency range is significantly steeper (~ -0.4, see Table 9).

For the Holdaway et al. (1994) counts, the situation is more complex. As they note in their paper, the exact form of the inverted-spectrum tail of their 8–90 GHz spectral-index distribution (which is poorly defined because of the small number of sources observed in this region) is very important, because it allows a small fraction of the numerous weak 5 GHz sources to be boosted up to very high flux densities at 90 GHz. Holdaway et al. (1994) do not discuss the effects of variability over the several-year interval between their 8- and 90-GHz data sets, but this could also scatter variable objects into the tail of their spectral-index distribution. Since our results and those of Waldram et al. (2007) agree well and are also based on higher-frequency (15–20 GHz) source-count data, we conclude that Holdaway et al. (1994) have overestimated the surface density of 95-GHz sources by up to a factor of 2.

5.5 Integrated source counts at 95 GHz

As a consistency check, we can use the differential source counts derived in the previous section to estimate the number of extragalactic radio sources brighter than a certain $S_{\rm lim}$ over the whole sky at 90–95 GHz:

$$N(S_{90} > S_{\rm lim}) = 4\pi \int_{S_{\rm lim}}^{+\infty} n(S)\,{\rm d}S. \quad (4)$$

Our results for $S_{\rm lim} = 0.1$ and 1.0 Jy are reported in Table 13 together with predictions from De Zotti et al. (2005) and Holdaway et al. (1994). Since the Waldram et al. (2007) counts are only valid for sources below 200 mJy, integrated source counts cannot be derived from their study.

Table 13. Comparison of the all-sky integrated source counts above a limiting flux density $S_{\rm lim}$ at the frequency ν between our predictions and the De Zotti et al. (2005) model and Holdaway et al. (1994) estimates. Our quoted errors have been derived from a Monte Carlo simulation based on the 20-GHz source counts and 20–95 GHz spectral-index distribution, and are dominated by the small-number statistics in the spectral-index distribution.

Source	ν	Integrated counts (all-sky)	
	(GHz)	>0.1 Jy	>1 Jy
This paper	95	2310 ± 1132	120 ± 64
De Zotti et al. (2005)	94	4457	288
Holdaway et al. (1994)	90	4400	178

Our derived source numbers are significantly lower than those derived by both De Zotti et al. (2005) and Holdaway et al. (1994). This is a reflection of the lower differential source counts found in our study, as discussed in the previous section. The actual number of sources stronger than 1 Jy over the whole sky at 90–95 GHz is still poorly determined, but the *WMAP* catalogue (Hinshaw et al. 2007) contains 106 sources which lie above this flux level at 94 GHz. The ATCA calibrator catalogue at declinations south of 0° contains 60 extragalactic sources stronger than 1 Jy in the 86–100 GHz band, implying roughly 120 such sources over the whole sky. Our derived value in Table 13 therefore appears reasonably consistent, within the errors, with what is observed.

5.6 Confusion noise in CMB surveys at 95 GHz

The 95-GHz source counts can also be used to compute the confusion noise $\sigma^2_{\rm conf}$ and the angular power spectrum δT_l of the temperature fluctuations due to discrete point-like extragalactic radio sources, seen as a small angular scale contamination to the CMB anisotropies. This study is complementary to the work described in the previous section, because once the brightest sources in the 90–100 GHz sky have been identified and removed from the CMB maps, the remaining fainter sources act as a confusing background. The formalism to derive σ^2 and δT_l is based on Cleary et al. (2005) and briefly described below.

Once a limiting flux density ($S_{\rm lim}$) for a survey at a certain observing frequency has been determined, the contribution to the temperature fluctuations from faint sources below that flux density limit has two components: one $C_{\rm src}^{\rm poisson}$ due to the Poisson-distributed sources and a second term due to clustering $C_{\rm src}^{\rm clustering}$:

$$T^2_{\rm CMB}\, C_{\rm src} = \left(\frac{\partial B_\nu}{\partial T}\right)^{-2} \left(C_{\rm src}^{\rm poisson} + C_{\rm src}^{\rm clustering}\right), \quad (5)$$

where $C_{\rm src}$ is the radio source angular power spectrum and

$$\frac{\partial B_\nu}{\partial T} = \frac{2k}{c^2} \left(\frac{k\,T_{\rm CMB}}{h}\right)^2 \frac{x^4\,\exp^x}{(\exp^x - 1)^2} \quad (6)$$

is the conversion factor between fluctuations in the background intensity and in antenna temperature. Here, k is the Boltzmann's constant and $x \equiv h\nu/kT_{\rm CMB}$, where $T_{\rm CMB} = 2.726$ K is the CMB mean temperature. The term $C_{\rm src}^{\rm poisson}$ given by the formula

$$C_{\rm src}^{\rm poisson} \equiv \sigma^2_{\rm conf} = \int_0^{S_{\rm lim}} S^2\, n(S)\,{\rm d}S \quad (7)$$

is also known as *confusion noise* for Poisson-distributed sources. This quantity is easy to estimate starting from experimental differential source counts $n(S)$.

The term for source clustering (Scott & White 1999) in equation (5) is given by

$$C_{\rm src}^{\rm clustering} = \omega_l \left[\int_0^{S_{\rm lim}} S\, n(S)\,{\rm d}S\right]^2, \quad (8)$$

where ω_l is the Legendre transform of the angular two-point correlation function of radio sources $\omega(\theta)$. Lacking any clear estimate of the clustering properties of extragalactic radio sources at the frequency of 90 GHz, we assume for now that this term is negligible.

In order to compare our prediction with others, we conventionally expressed the point-source angular power spectrum in terms of the

Table 14. Comparison between the normalization coefficient A of temperature fluctuation angular power spectrum due to the background of extragalactic discrete point-like sources fainter then 1 Jy at the observing frequency ν.

Author	ν (GHz)	A (μK)
This paper	95	0.78
De Zotti et al. (2005)	94	1.12
Toffolatti et al. (1998)	100	1.0
Giommi et al. (2006)	94	1.3

Legendre multiple coefficient l:

$$\Delta T^2_{\rm src} = T^2_{\rm CMB} \frac{l(l+1)\, C_{\rm src}}{2\pi} \approx \text{constant} \times \left(\frac{l}{100}\right)^2 \quad (9)$$

so that δT_l is simply given by

$$\delta T_l = \left(\Delta T^2_{\rm src}\right)^{1/2} \approx A \times \frac{l}{100}. \quad (10)$$

The normalization coefficient A of the angular power spectrum δT_l obtained from our 95-GHz predicted counts is shown in Table 14 together with the model by Toffolatti et al. (1998), the model by De Zotti et al. (2005) which includes the contribution of flat-spectrum radio quasars, BL Lacs and steep-spectrum radio galaxies and the estimate by Giommi et al. (2006) for the blazar population only. In our computation of δT_l, we assumed that the 95-GHz counts keep the same functional form for $S_{95} < 82$ mJy, which is the effective 95-GHz limit for our target sample.

6 SUMMARY AND FUTURE WORK

In this study, we have shown that the ATCA can measure robust 95-GHz (3-mm) flux densities for relatively faint continuum sources in a few minutes of integration time, provided that careful attention is given to calibrating the telescope pointing. Our ATCA measurements at 20 and 95 GHz appear to be on the same flux scale as the *WMAP* catalogue (Hinshaw et al. 2007) to within the errors. The arrival in 2008 of the new ATCA broad-band correlator, which has a 2 GHz bandwidth compared to the present value of 128 MHz, will significantly increase the continuum sensitivity at 95 GHz and should make it possible to measure 95-GHz sources down to $\sim$10 mJy with integration times similar to those used here.

We have made a new estimate of the 95-GHz radio source counts for sources stronger than 80 mJy, and show that some previous studies have overestimated the number of these sources by up to a factor of 2. In particular, the confusion level in the *Planck* beam at 95 GHz is likely to be significantly lower than previously estimated.

Fewer than half the sources in our 95-GHz sample presently have measured redshifts, and obtaining good-quality optical spectra for the whole sample would be valuable both to study their rest-frame radio spectra and to test whether the brightest 95-GHz sources are relativistically beamed in the optical, as suggested in Section 4.8.

We plan to make new measurements of a complete sample of sources from the AT20G Bright Source Sample (Massardi et al. 2008) at 20, 40 and 95 GHz in late 2007, using the new ATCA 7-mm receiver system. These observations, which will also include polarization measurements, should provide further insights into the properties of the strongest 95-GHz sources.

ACKNOWLEDGMENTS

We thank the staff at the ATCA for their support during our observing runs, and the AT20G and 6dFGS teams for making their data available to us in advance of publication. We also acknowledge the support of the Australian Research Council through the award of an ARC Australian Professorial Fellowship to EMS and a Federation Fellowship to RDE.

The ATCA is part of the Australia Telescope, which is funded by the Commonwealth of Australia for operation as a National Facility managed by CSIRO. This research has made use of the NED which is operated by the Jet Propulsion Laboratory, California Institute of Technology, under contract with the National Aeronautics and Space Administration. This research has also made use of data obtained from the SuperCOSMOS Science Archive, prepared and hosted by the Wide Field Astronomy Unit, Institute for Astronomy, University of Edinburgh, which is funded by the UK Particle Physics and Astronomy Research Council.

We thank the referee, Prof. Ian Browne, for a prompt and very helpful report.

REFERENCES

Baker J. C., Hunstead R. W., 1995, ApJ, 452, L95
Bennett C. L. et al., 2003, ApJ, 583, 1
Bock D. C-J., Large M. I., Sadler E. M., 1999, AJ, 117, 1593
Bolton R. C. et al., 2004, MNRAS, 354, 485
Browne I. W. A., Wright A. E., 1985, MNRAS, 213, 97
Cleary K. A. et al., 2005, MNRAS, 360, 340
Cohen A. S., Lane W. M., Cotton W. D., Kassim N. E., Lazio T. J. W., Perley R. A., Condon J. J., Erickson W. C., 2007, AJ, 134 1245
Colless M. et al., 2001, MNRAS, 328, 1039
Condon J. J., 1984, ApJ, 287, 461
Condon J. J., Cotton W. D., Greisen E. W., Yin Q. F., Perley R. A., Taylor G. B., Broderick J. J., 1998, AJ, 115, 1693
Cornwell T. J., 1987, A&A, 180, 269
De Breuck C., 2005, in Wilson A., ed., ESA SP-577, Proc. The Dusty and Molecular Universe: A Prelude to HERSCHEL and ALMA. ESA Publications Division, Noordwijk, p. 27
De Zotti G., Ricci R., Mesa D., Silva L., Mazzotta P., Toffolati L., Gonzalez-Nuevo J., 2005, A&A, 431, 893
Giommi P., Colafrancesco S., Cavazzuti E., Perri M., Pittori C., 2006, A&A, 445, 855
Gregory P. C., Scott W. K., Douglas K., Condon J., 1996, ApJS, 103, 427
Griffith M. R., Wright A. E., 1993, AJ, 105, 1666
Hambly N. C. et al., 2001, MNRAS, 326, 1279
Hinshaw G. et al., 2007, ApJS, 170, 288
Holdaway M. A., Owen F. N., Rupen M. P., 1994, Millimeter Array Memo #123, Source Counts at 90 GHz, http://www.alma.nrao.edu/memos
Holdaway M. A., Carilli C., Laing R., 2004. ALMA memo #493, Finding Fast Switching Calibrators for ALMA. http://www.alma.nrao.edu/memos
Hovatta T., Tornikoski M., Lainela M., Lehto H. J., Valtaoja E., Torniainen I., Aller M. F., Aller H. D., 2007, A&A, 469, 899
Jones D. H. et al., 2004, MNRAS, 355, 747
Kellermann K. I., 1964, ApJ, 140, 969
Kellermann K. I., Pauliny-Toth I. I. K., Davis M. M., 1968, Astrophys. Lett., 2, 105
Kesteven M., 1998, ATNF Technical Memo AT/39.3/081, ATCA upgrade – Pointing considerations, http://www.atnf.csiro.au/projects/mnrf1996/technical_memos
Lähteenmäki A., Valtaoja E., 1999, ApJ, 521, 493
Lamarre J. M. et al., 2003, New Astron.Res., 47, 1017
Landau R., Epstein E. E., Rather J. D. G., 1980, AJ, 85, 363
López-Caniego M., Herranz D., González-Nuevo J., Sanz J. L., Barreiro R. B., Vielva P., Argüeso F., Toffolatti L., 2006, MNRAS, 370, 2047

Lowe S. R., Gawronski M. P., Wilkinson P. R., Kus A. J., Browne I. W. A., Padzerski E., Feiler R., Kettle D., 2007, A&A, 474, 1093
Massardi M. et al., 2008, MNRAS, 384, 775
Mauch T., Murphy T., Buttery H. J., Curran J., Hunstead R. W., Piestrzynski B., Robertson J. G., Sadler E. M., 2003, MNRAS, 342, 1117
Middelberg E., Sault R. J., Kesteven M. J., 2006, PASA, 23, 147
O'Dea C. P., 1998, PASP, 747, 493
Owen F. N., Mufson S. L., 1977, AJ, 82, 776
Owen F. N., Porcas R. W., Mufson S. L., Moffett T. J., 1978, AJ, 83, 685
Owen F. N., Helfand D. J., Spangler S. R., 1981, ApJ, 250, L55
Patnaik A. R., Browne I. W. A., Wilkinson P. N., Wrobel J. M., 1992, MNRAS, 254, 655
Rengelink R. B., Tang Y., de Bruyn A. G., Miley G. K., Bremer M. N., Röttgering H. J. A., Bremer M. A. R., 1997, A&AS, 124, 259
Ricci R. et al., 2004, MNRAS, 354, 305
Sault R. J., Teuben P. J., Wright M. C H., 1995, in Shaw R. A., Payne H. E., Hayes J. J. E., eds, ASP Conf. Ser. Vol. 77, Astronomical Data Analysis Software and Systems IV. Astron. Soc. Pac., San Francisco, p. 433
Sadler E. M. et al., 2006, MNRAS, 371, 898
Scott D., White M., 1999, A&A, 346, 1
Snellen I. A. G., Schilizzi R. T., Miley G. K., de Bruyn A. G., Bremer M. N., Röttgering H. J. A., 2000, MNRAS, 319, 445
Steppe H., Salter C. J., Chini R., Kreysa E., Brunswig W., Lobato Perez J., 1988, A&AS, 75, 317
Teräsranta H. et al., 2004, A&A 427, 769
Thompson A., Moran J. M., Swenson G. W., 2001, Interferometry and Synthesis in Radio Astronomy, 2nd edn. Wiley, New York
Tinti S., De Zotti G., 2006, A&A, 445, 889
Toffolatti L., Argueso Gomez F., de Zotti G., Mazzei P., Franceschini A. et al., 1998, MNRAS, 297, 117
Voss H., Bertoldi F., Carilli C., Owen F. N., Lutz D., Holdaway M., 2006, A&A, 448, 823
Waldram E. M., Pooley G. G., Grainge K. J. B., Jones M. E., Saunders R. D. E., Scott P. F., Taylor A. C., 2003, MNRAS, 342, 915
Waldram E. M., Bolton R. C., Pooley G. G., Riley J. M., 2007, MNRAS, 379, 1442

APPENDIX A: NOTES ON INDIVIDUAL SOURCES

(i) *0058−3234*. The 6dFGS spectrum (Jones et al. 2004) shows a bright featureless continuum and no redshift could be measured.

(ii) *0111−4749*. The optical ID is a 2dFGRS (Colless et al. 2001) galaxy at $z = 0.154$ whose spectrum shows strong, narrow emission lines. This is one of the few AT20G sources in our sample which was undetected at 95 GHz. The radio spectrum rises steeply from 0.8 to 20 GHz, and so must peak somewhere above 20 GHz. The 843-MHz SUMSS images show extended emission with a deconvolved largest angular size of 83 arcsec at PA 36°.

(iii) *0136−4044*. This appears to be the same object as PMNJ 0136−4044, though the catalogued PMN position is significantly offset from the more accurate AT20G radio position. There is a faint (stellar) optical ID at the AT20G position.

(iv) *0142−4206*. This source appears extended in the 843-MHz SUMSS image (deconvolved major-axis 59 arcsec at PA 25°).

(v) *0245−4459*. The 6dFGS spectrum shows strong, broad Balmer emission lines typical of a Seyfert 1 galaxy or QSO.

(vi) *0320−3837*. This source is so close to a bright star that no optical ID is possible.

(vii) *0428−4357*. Blank field on the blue DSS image. No known optical ID.

(viii) *0433−4502*. One of the few sources in our sample which shows an inverted radio spectrum at all frequencies from 0.8 to 95 GHz. The DSS optical ID is a 19th magnitude galaxy whose redshift is presently unknown.

(ix) *0440−4731*. This source is well below the limit of the SUMSS catalogue at 843 MHz, but an examination of the original SUMSS image shows a marginal (3σ) detection of a 2.5-mJy source at the AT20G position. There is no optical ID, and this is one of the few AT20G sources which does not appear in any previous optical or radio catalogue.

(x) *0523−2955*. This source is extended (or perhaps confused) in the SUMSS image (deconvolved major-axis 47 arcsec at PA 141°). The NVSS image also shows extended emission with largest angular size of 56 arcsec.

(xi) *0608−3041*. This source is clearly extended north-south in the SUMSS image (deconvolved major-axis 92 arcsec at PA 1°), and an extended structure is also clearly seen in the AT20G 5-GHz image even though the image quality is poor in this snapshot observation. The 1.4-GHz NVSS resolves the source into two components separated by about 70 arcse. At 20 GHz the source is unresolved. The 6dFGS spectrum shows strong, broad Balmer emission lines typical of a Seyfert 1 galaxy or QSO. At $z = 0.2237$, this is a relatively nearby object.

(xii) *1117−4837*. This source is extended in the SUMSS image (deconvolved major-axis 47 arcsec at PA 75°).

(xiii) *1427−3305*. The 6dFGS spectrum shows a featureless continuum, and no redshift could be measured. The optical counterpart is stellar on the blue DSS image, but is fuzzy (and classified as a galaxy) on the red image, suggesting that this may be a relatively nearby BL Lac object.

(xiv) *1454−3747*. The 6dFGS spectrum shows strong, broad Balmer emission lines typical of a Seyfert 1 galaxy or QSO.

(xv) *2031−3647*. The 6dFGS spectrum shows emission lines of C III] and Mg II.

(xvi) *2113−3838*. The 6dFGS spectrum shows a strong blue continuum with a single broad emission line of Mg II.

(xvii) *2113−3838*. The 6dFGS spectrum shows strong, broad emission lines of Hγ and Mg II.

This paper has been typeset from a TEX/LATEX file prepared by the author.